iScience

Article

Cardiac fibrosis inhibitor CTPR390 prevents structural and morphological changes in human engineered cardiac connective tissue

Graphical abstract

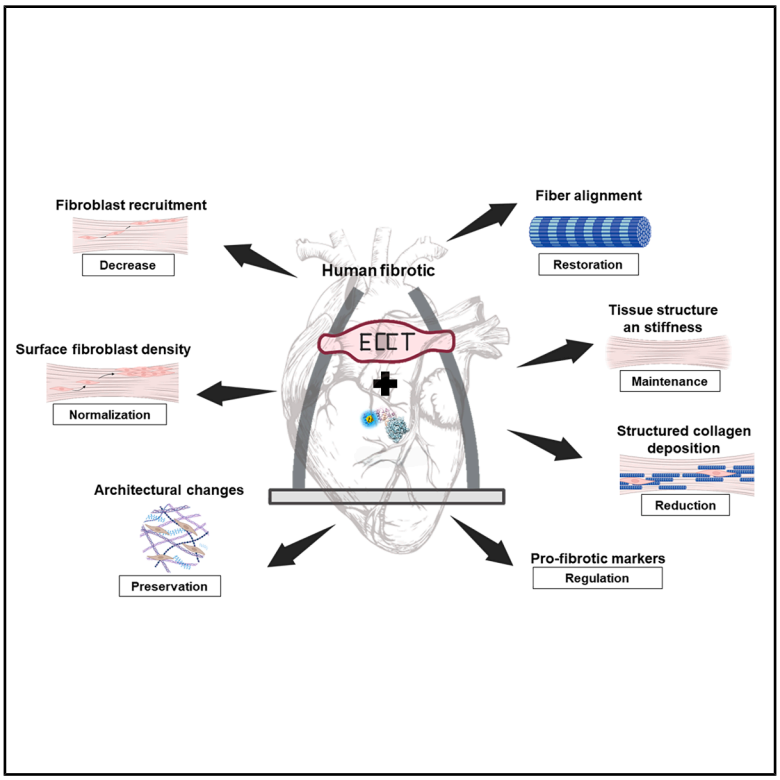

Authors

David Maestro, Ana Palanca, Helena Soto, ..., Susanne Lutz, Aitziber L. Cortajarena, Ana V. Villar

Correspondence

villarav@unican.es

In brief

Molecular biology; Cell biology

Highlights

- CTPR390 prevented architectural changes in TGFβ1-activated ECCT
- CTPR390 preserves tissue perimeter, collagen fibers alignment
- CTPR390 reduces structured areas and degree of collagen structuration
- CTPR390-trested ECCTs presented a biomechanical behavior similar to control ECCT

Maestro et al., 2025, iScience *28*, 113013
August 15, 2025
https://doi.org/10.1016/j.isci.2025.113013

CellPress

iScience

CellPress
OPEN ACCESS

Article

Cardiac fibrosis inhibitor CTPR390 prevents structural and morphological changes in human engineered cardiac connective tissue

David Maestro,[1] Ana Palanca,[2] Helena Soto,[1,9] I. Llarena,[3] Alisa Nicole DeGrave,[4,5] Gabriela Guedes,[3] Guilherme Henrique de Oliveira,[6] André Luiz Coelho Conceição,[7] Verónica Mieites,[8,9] Jose M. Icardo,[2] Carlos Sanchez-Cano,[6,10,11] Olga M. Conde,[8,9,12] Susanne Lutz,[4,5] Aitziber L. Cortajarena,[3,11] and Ana V. Villar[1,13,14,*]

[1]Instituto de Biomedicina y Biotecnología de Cantabria (IBBTEC), Consejo Superior de Investigaciones Científicas (CSIC)-Universidad de Cantabria (UC), Santander, Spain
[2]Departamento de Anatomía y Biología Celular, Universidad de Cantabria, Santander, Spain
[3]Center for Cooperative Research in Biomaterials (CIC biomaGUNE), Basque Research and Technology Alliance (BRTA), Paseo de Miramón 194, 20014 Donostia-San Sebastián, Spain
[4]Institute of Pharmacology and Toxicology, University Medical Center, Goettingen, Germany
[5]DZHK (German Centre for Cardiovascular Research) Partner Site, Goettingen, Germany
[6]Donostia International Physics Center, Manuel Lardizabal Ibilbidea 4, 20018 Donostia, Spain
[7]Deutsches Elektronen-Synchrotron DESY, Notkestr. 85, 22607 Hamburg, Germany
[8]Photonics Engineering Group, University of Cantabria, 39005 Santander, Spain
[9]Valdecilla Biomedical Research Institute (IDIVAL), 39011 Santander, Spain
[10]Ikerbasque, Basque Foundation for Science, 48009 Bilbao, Spain
[11]Polimero eta Material Aurreratuak: Fisika, Kimika eta Teknologia, Kimika Fakultatea, Euskal Herriko Unibertsitatea UPV/EHU, 20018 Donostia-San Sebastian, Spain
[12]CIBER-BBN, Biomedical Research Networking Center—Bioengineering, Biomaterials, and Nanomedicine, Avda. Monforte de Lemos 3–5, Pabellón 11, Planta 0, 28029 Madrid, Spain
[13]Departamento de Fisiología y Farmacología, Facultad de Medicina, Universidad de Cantabria, Santander, Spain
[14]Lead contact
*Correspondence: villarav@unican.es
https://doi.org/10.1016/j.isci.2025.113013

SUMMARY

Cardiac fibrosis is a key characteristic of heart failure. CTPR390, an experimental anti-fibrotic inhibitor targeting Hsp90, has shown success in animal models, but remains unexplored in human cardiac models. This study evaluated an engineered cardiac connective tissue (ECCT) model, focusing on changes in the extracellular matrix and fibroblasts. Results showed that CTPR390 prevented architectural changes in TGFβ1-activated ECCT, preserving tissue perimeter, collagen fibers alignment while reducing structured areas and degree of collagen structuration. CTPR390 treatment reduced cell area of fibroblasts under tension, without changes in the internal rounded cells devoid of tension. Fibroblast recruitment to tension areas was diminished, showing biomechanical behavior similar to control ECCT. This treatment also lowered the gene and protein expression of key pro-fibrotic markers. Here, advanced biotechnology was employed to detect the detailed structure of tissue fibrosis reduction after administering CTPR390, representing a significant advancement toward clinical application for cardiac fibrosis treatment.

INTRODUCTION

Cardiovascular disease remains the leading cause of death in industrialized countries, contributing significantly to morbidity and mortality. Cardiac fibrosis emerges as a secondary occurrence in various cardiovascular diseases, constituting a pathological condition.[1] Although initially intended to safeguard the heart's function following myocardial damage, it contributes to the expansion of the cardiac interstitium by depositing an excess of extracellular matrix (ECM) proteins, ultimately leading to a loss of function. There are three distinct forms of cardiac fibrosis: (1) Replacement fibrosis: This occurs after myocardial infarction where necrotic cardiomyocytes are replaced by a collagen-based scar. (2) Perivascular fibrosis: In this form, the microvascular adventitia undergoes expansion. (3) Interstitial fibrosis: This type involves the abnormal increase in the endomysial and perimysial spaces due to the excessive accumulation of ECM proteins in the absence of significant cardiomyocyte loss. Interstitial fibrosis can occur in response to various cardiovascular conditions such as aortic valve dysfunction or hypertension. An increase in fibrosis leads to increased tissue stiffness primarily due to excessive deposition of collagen and other structural

proteins. As fibrosis progresses, cross-linking between collagen fibers increases, making the ECM more rigid and resistant to deformation. Additionally, the loss of normal ECM remodeling impairs tissue elasticity, further contributing to stiffness.[2] This increased stiffness affects cellular behavior, potentially worsening fibrosis by promoting further ECM production and altering mechanotransduction pathways. This stiffness can contribute to adverse effects such as exacerbation of dilation, contractile diastolic dysfunction, and the progression to heart failure. Therefore, the extent of cardiac fibrosis is considered a predictor of adverse outcomes in patients with heart disease.[1] Despite extensive research on heart disorders, such as cardiac fibrosis, there is an absence of therapies that address and reverse heart disease.[3] One of the challenges impeding progress in cardiovascular therapy development is the absence of self-organizing human cardiac models that recapitulate key aspects of human heart disease.[4] While animal models are employed to investigate the chronology of cardiac events in response to specific stressors over time and offer insights into remodeling patterns,[5–7] there is a recognition of the differences between mice and humans. Moreover, in patients, the majority of clinical knowledge about cardiac diseases progression is either retrospective or derived from late-stage patients, identified only after years of remodeling precipitates symptoms. Multiple formats of engineered heart muscle have been created for the study of cardiac diseases. Examples include engineered human myocardium (EHM) models generated using human induced pluripotent stem cell-derived cardiomyocytes (hiPSC-CD) or human embryonic stem cell-derived cardiomyocytes and collagen,[8] and human engineered heart tissue (EHT) using hiPSC-CD and human stromal cells.[9,10] These models, which mimic the complexity and functionality of heart tissue, are designed for various research and therapeutic purposes.[4] There is also a simpler model called engineered cardiac connective tissue (ECCT) that includes human cardiac fibroblasts embedded in collagen hydrogels and mimics the three-dimensional architecture of the adult cardiac fibroblast environment. The ECCT model is ideal for studying various characteristics of fibrotic diseases in the adult heart.[11,12] ECCT models, incorporating human cardiac fibroblasts in collagen hydrogels, effectively mimic the 3D architecture of adult cardiac fibroblasts, making them ideal for studying fibrotic diseases.[13] ECCT presents the advantage of mimicking areas of high density fibroblast which overexpress ECM during the pathological remodeling of the heart. The study of those fibrotic niches are of interest to understand the building and maintaining the physiological structural integrity.[14] Fibroblasts niches environments that support housekeeping function engaging intercellular cross talk are mimicked by the ECCT system and allowed us to study cardiac homeostasis protect by administering specific drugs. EHM or EHT models, mimic other cardiac environments allowing the focus of the study on different cardiac cell type interaction, which are also of great interest for the understanding of interaction between cell types in the heart essential for the coordinated function of the tissue.

Understanding ultrastructural changes in the fibrotic ECM, such as fiber alignment,[15] and collagen scar,[16] is crucial for evaluating advanced treatments. This study employs ECCT to explore mechanical, biochemical, and ultrastructural characteristics of fibroblasts and ECM fibers exposed to an experimental anti-fibrotic nanodrug. ECCT fibrosis is induced by transforming growth factor β (TGFβ),[17] a cytokine secreted by fibroblasts.[18] TGFβ initiates the pro-fibrotic process,[19] and activates its receptor complex on the cell surface. Disrupting TGFβ signaling in cardiac fibroblasts has been linked to fibrosis reduction.[20,21] Heat shock protein 90 (Hsp90), an ATP-dependent molecular chaperone, aids protein folding. Inhibiting Hsp90 with commercial Hsp90 inhibitors, such as 17AAG or Geldanamycin, which address the N-terminal end of Hsp90 are used in cancer and lead to cell death exhibiting ocular- and cardio-toxicity.[22,23] Inhibition in Hsp90 C-terminal end, can reduce TGFβ signaling activity.[24] These approaches include the reduction of TGFβ signaling activity by disrupting the TGFβ receptor complex involving Hsp90.[20] One such C-terminal end Hsp90 inhibitor tested as an anti-fibrotic molecule that maintain cell homeostasis is the engineered consensus tetratricopeptide repeat inhibitor of Hsp90 (CTPR390).[20,25,26] The advantages of CTPR390 over other Hsp90 inhibitors is based on its mechanism of action that inhibits Hsp90-TGFβ receptor I binding instead avoiding its chaperon function which drastically reduces cell homeostasis. Cell homeostasis reduction could be a strategy in cancer treatments but needs to be avoid in the case of cardiac treatments. Two key characteristics make CTPR390 an increasingly promising translational anti-fibrotic therapy. First, its proven anti-fibrotic effect in the fibrotic mouse heart.[20,25] Second, its protein-like structure, which may result in a lower immune response compared to other clinical treatments. The protein region of CTPR390 (ProtCTPR390) consists of three consensus tetratricopeptide repeat (CTPR) units repeated in tandem, which were engineered drawing inspiration from natural binding domains like tetratricopeptide repeats (TPR) found in proteins such as Hsp70/Hsp90 organizing protein (HOP).[27] Through genetic manipulation, ProtCTPR390 was combined with other functional motif, i.e., a gold nanocluster (AuNC) coordinating domain[28] designed to display cysteines at strategic locations, creating multifunctional chimeric proteins.[29,30] These proteins were additionally conjugated with Alexa 488, resulting in stable, trackable constructions under biological conditions through nanocluster or fluorophore-specific imaging while harboring the active module capable of binding to Hsp90.[31–33] The binding occurs at the C-terminal end of Hsp90, thus inhibiting the interaction of Hsp90 with the TGFβ receptor complex, which disrupts the proper functioning of the TGFβ-dependent fibrosis signaling cascade.[20,25]

The TGFβ-activated ECCT from cardiac patient fibroblasts offers a model to explore biomechanical and biochemical responses to advanced anti-fibrotic drugs like CTPR390. Additionally, it presents an opportunity to reveal, in a human 3D model and using advanced technology, various ultrastructural features of human cardiac collagen and fibroblast behavior following an anti-fibrotic action.

RESULTS

CTPR390 restores physical and biomechanical properties of fibrotic ECCTs

Our primary objective in this study was to investigate the impact of a well-established *in vitro* and *in vivo* anti-fibrotic protein

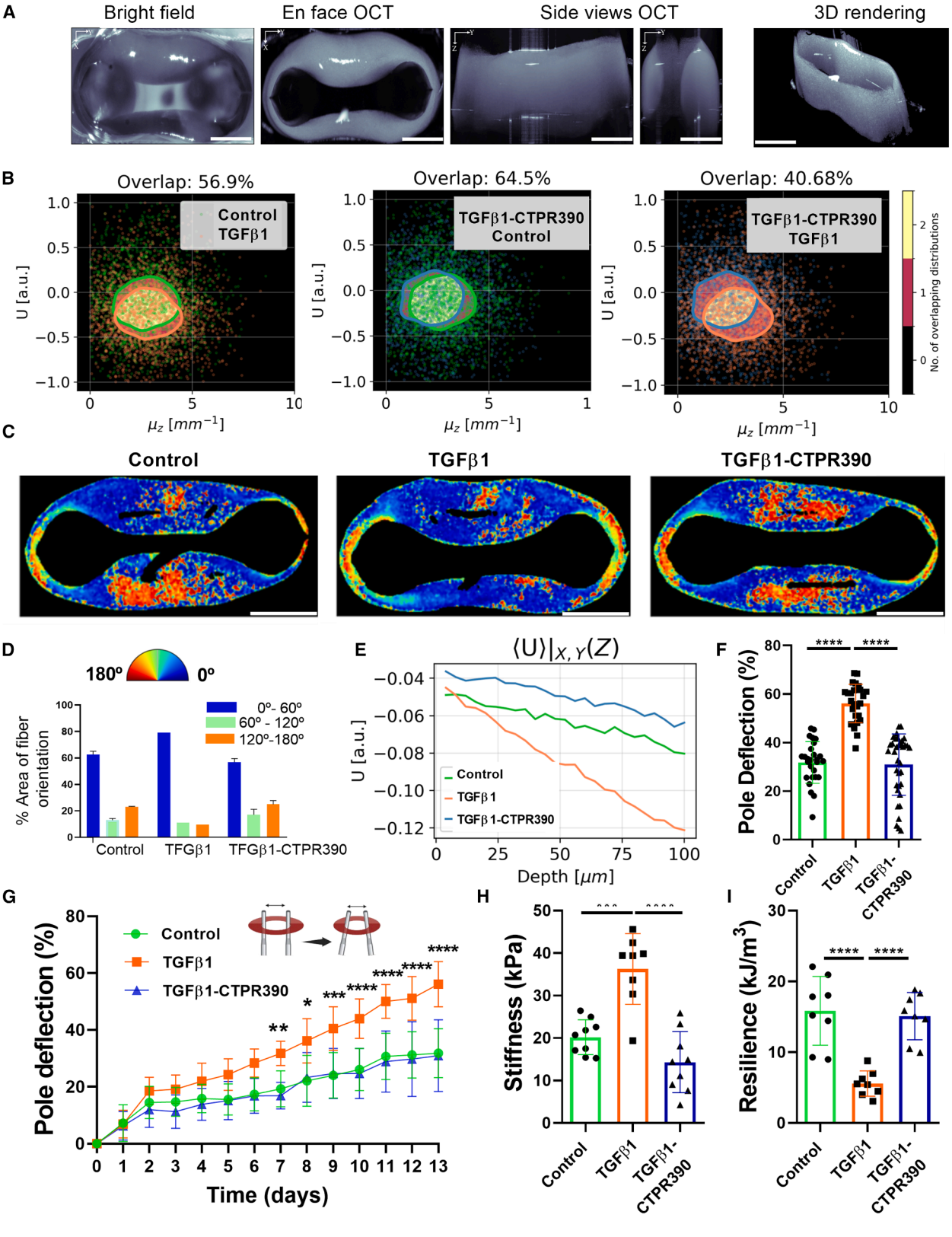

(legend on next page)

hybrid system (CTPR390)[20,25,34] on the physical and biomechanical properties of human tissue. We confirmed the optimum characteristics of the CTPR390 batch used in this study. The final molecule contains its characteristic Hsp90 binding module, the Alexa 488 fluorophore, and the Au nanocluster. We generated ECCT composed of primary adult cardiac fibroblasts and bovine collagen I within molds equipped with flexible poles (Figure 1A). Polarization-Sensitive Optical Coherence Tomography (PS-OCT) distinguishes itself as a method with significant potential for offering a comprehensive depiction of the morphological architecture of tissues. The PS-OCT provided detailed images of the ECCT structure showing both top-down and side views (Figure 1A). Three groups of ECCTs were cultured for 13 days: Control, TGFβ1 (ECCTs cultured in the presence of TGFβ1 to induce fibrosis), and TGFβ1-CTPR390 (TGFβ1 ECCTs cultured in the presence of CTPR390 to prevent fibrosis). CTPR390 was engineered with an Hsp90 binding module and Alexa 488 fluorophore for visualization, and its purity, stability (Figure S1A) and molecular weight (Figures S1A and S1B) were confirmed. The folding, stability signatures of CTPR390-AuNC (Figure S1C) and the emission spectra of CTPR90-AuNC-488 named CTPR390 (Figures S1C–S1F) were also verified. The concentration of TGFβ1 used in this study was consistent with the one previously employed in this model to induce fibrosis.[17] All three ECCT groups exhibited the potential for longitudinal tissue contraction.[17] The optimal anti-fibrotic concentration of CTPR390 was previously established to be 1 μM based on the extrapolation of titration assays conducted in primary fibroblasts.[20] We confirmed that the Control-CTPR390 group, in which CTPR390 was administered without TGFβ1, exhibited similar cell viability and pro-fibrotic gene expression to the Control group (Figures S2B and S2C). Furthermore, our previous findings demonstrated that *in vivo* administration of CTPR390 did not affect the gene expression of TGFβ1, COL I A1, COL III A1, or Smad2/3 in the hearts of Sham mice.[20] Based on these results, we decided to exclude the Control-CTPR390 group from the rest of analysis of the present study.

To evaluate differences in the physical characteristics among the three ECCT groups under study, we created dispersion maps of their co-registered optical properties to compare conditions. Figure 1B showed the response of light given by the attenuation coefficient (x axis) as it passes through a tissue with different internal organization. We derived the polarization properties through the Stokes parameters, of which parameter U is represented in the y axis. As both the attenuation and Stokes parameters are derived pixel-wise, we evaluated their mutual relationship (Figure 1B). The two-dimensional distributions of Control/TGFβ1-CTPR390 ECCTs (64.5% overlap) differed in the x axis, indicating a change in attenuation. This suggests that, while similar, the TGFβ1-CTPR390 ECCT has internal structures of different sizes compared to those of the Control group. On the other hand, Control/TGFβ1 (56.9% overlap) differed in the y axis, suggesting a change in tissue organization as given by the polarization properties, without a change of size of the internal structures (their attenuation was similar). As the TGFβ1-CTPR390 has a different scattering response, and the TGFβ1 has a different polarization response, the two groups had the smallest overlap between them, corresponding to a 40.7%

Figure 1. Administering CTPR390 to TGFβ1-activated ECCT resulted in a reversal of its physical and biomechanical characteristics to those observed in control ECCT

(A) Representative images (bright field image, *en face* view, side views, and 3D rendering) of an ECCT using PS-OCT technique that showed the morphology of the engineered tissue around the two flexible poles. The white scale bar indicated 1.3 mm.

(B) Three panels showing the correlative behavior observed within a sigma area between the Stokes U and the attenuation coefficient (μm^{-1}), considering the quantified overlap in distributions in Control, TGFβ1, and TGFβ1-CTPR390 ECCT samples. n = 3 biological samples (ECCT) measuring 10^8 pixels in triplicate distributed in layers of 3 3.6 μm/px thick, assuming a refractive index of n = 1.38, typical of biological samples, evaluated up to the first 100 micrometers. White scale bar indicated 1 mm.

(C) Representative ECCT images of the angle of polarization (AoP) orientation aligned with the fibers within the ECCT using the same color-coding as in panel. n = 3 biological samples (ECCT) measuring 10^8 pixels in triplicate distributed in layers of 3 3.6 μm/px thick, assuming a refractive index of n = 1.38, typical of biological samples, evaluated up to the first 100 micrometers in Control, TGFβ1 and TGFβ1-CTPR390 groups. The white scale bar indicated 1.3 mm.

(D) Bar graph illustrating the quantification of areas with the same percentage of AoP aligned with ECCT fibers, using the PS-OCT technique. AoP color code: blue (0° – 60°), green (60° – 120°), and orange (120° – 180°). The process from data acquisition segmenting areas with the same AoP and assigning the color code for the AoP is detailed in Figure S2A. n = 2 biological samples (ECCT) measuring 10^8 pixels in triplicate distributed in layers of 3.6 μm/px thick, assuming a refractive index of n = 1.38, typical of biological samples, evaluated up to the first 100 micrometers.

(E) Evolution along depth (z) of the xy-averaged Stokes U parameter (a.u.) among the Control, TGFβ1, and TGFβ1-CTPR390 groups within the initial 100 μm from the surface of the ECCT. Control Y = (−554.8e-04 ± 8.0e-04) + (−129.8e-05 ± 5.7e-05) X. TGFβ1 Y = (−525.7e-04 ± 8.1e-04) + (−362.1e-05 ± 5.8e-05) X. TGFβ1-CTPR390 Y = (−431.9e-04 ± 8.0e-04) + (−138.3e-05 ± 5.7e-05) X. n = 3 biological samples (ECCT) measuring 10^8 pixels in triplicate distributed in layers of 3 3.6 μm/px thick, assuming a refractive index of n = 1.38, typical of biological samples, evaluated up to the first 100 micrometers.

(F) Detailed analysis of contraction at day 13 presented in a bar graph comparing Control and TGFβ1-CTPR390, to TGFβ1 group. Values presented as means ± SEM for n = 12 ECCT per group with triplicates of each biological sample (****p < 0.0001) were assessed through two-way ANOVA with Tukey's multiple comparison test.

(G) ECCT contraction was evaluated over a 13-day period based on the percentage (%) of pole deflection in three groups (Control, TGFβ1, and TGFβ1-CTPR390), n = 12 ECCT per group with triplicates of each biological sample.

(H) Bar graph illustrating ECCT stiffness (Young's modulus) with significant differences observed in TGFβ1 compared to Control or TGFβ1-CTPR390 groups n = 8–9 ECCT per group with triplicates of each biological sample.

(I) Bar graph depicting ECCT resilience with significant differences noted in TGFβ1 compared to Control or TGFβ1-CTPR390 groups, n = 7–9 ECCTs with triplicates of each biological sample. All datasets, except for (F), passed the Shapiro-Wilk test for normal distribution. p-values for datasets following a normal distribution (*p < 0.05, **p < 0.005, ***p < 0.0005, ****p < 0.0001) were determined using one-way ANOVA with Tukey's multiple comparison test. For (F), where the dataset did not follow a normal distribution, p-values (****p < 0.0001) were determined using the non-parametric Mann-Whitney test. In all graphs, error bars represent the variability of the data as standard deviation.

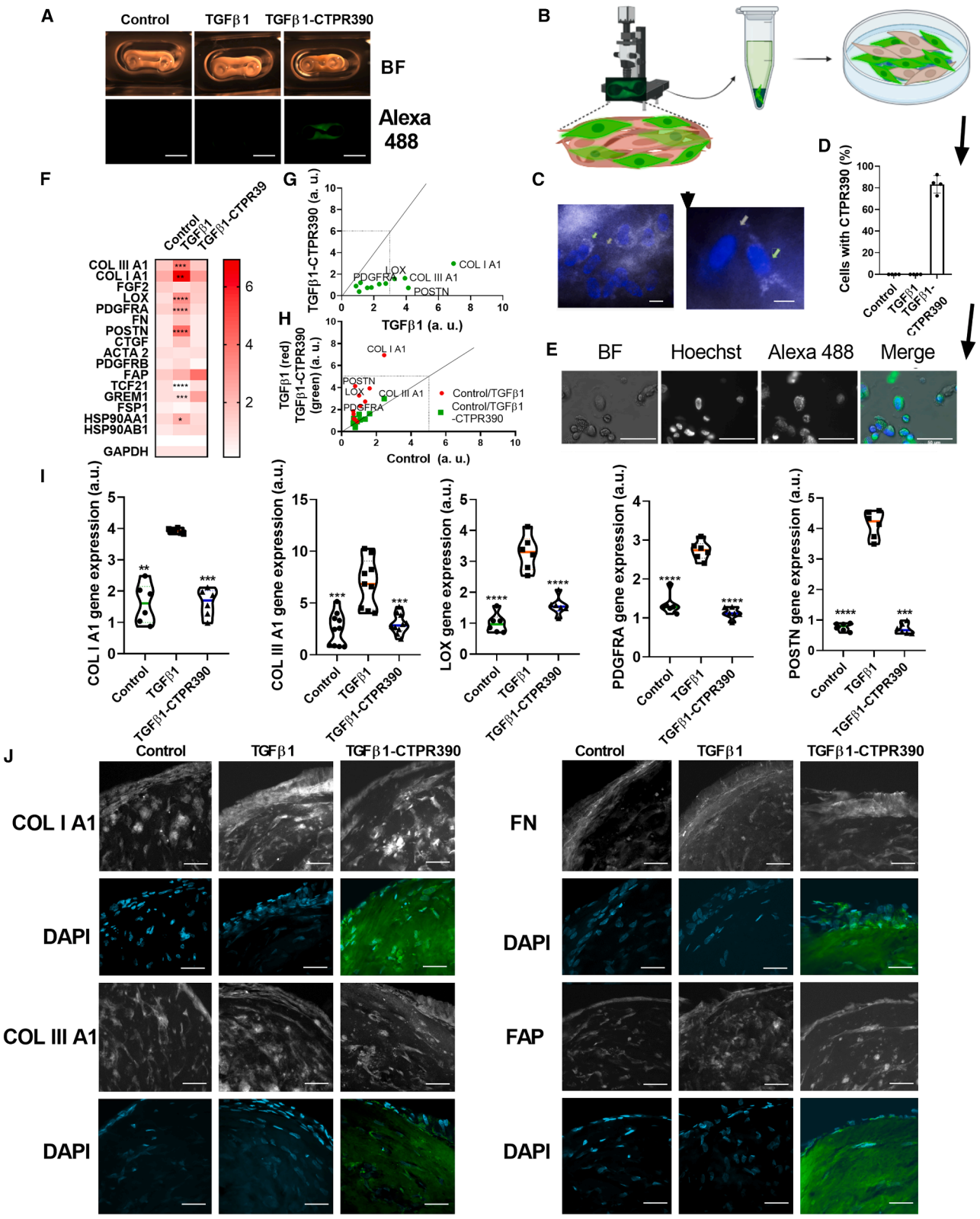

(legend on next page)

overlap (Figure 1B). The combination of imaging contrasts and detailed ECCT 3D microarchitecture enabled the acquisition of information on the orientation of the angle of polarization (AoP) at a depth of 100 μm (Figures 1C and 1D). Moreover, fiber orientation analysis revealed that CTPR390 prevented fibrosis, producing fiber alignment similar to the control with fewer fibers at angles above 120°, while TGFβ1 led to highly structured fibers more aligned at angles below 60° (Figures 1C and 1D). The process from data acquisition segmenting areas with the same AoP and assigning the color code for the AoP is detailed in (Figure S2A). We also measured tissue organization along depth (z), with TGFβ1 showing a decline in fiber alignment, which was corrected by CTPR390, bringing it closer to control levels (Figure 1E). These measurements revealed distinct differences in the amount of polarized light traveling parallel to the +/− 45° axes with respect to the horizontal of the images when comparing the fibrotic condition to the Control and TGFβ1-CTPR390 ECCTs than between Control and TGFβ1, or TGFβ1-CTPR390 and TGFβ1 ECCTs conditions. The steady rate of change along depth corresponding to a linear relationship between U and z indicates some level of fiber uniformity (overall change below −10% for all samples), with steeper slopes being markers of higher fiber alignment between different layers of the sample (Figure 1E). Biomechanical analysis over 13 days showed increased contraction in TGFβ1-treated ECCTs from day 7, while TGFβ1-CTPR390 condition prevented these changes, maintaining control group behavior (Figures 1F and 1G). Every day measurements of pole deflection revealed a significant increase in the contraction capabilities of TGFβ1 compared to Control group starting from day 7 (Figure 1G). The Young's Modulus, reflecting ECCT stiffness, was determined from the stress-strain curves and those measurements unveiled a significant increase in stiffness of TGFβ1 group compared to Control group (***$p < 0.0005$), which was prevented by co-application of CTPR390 (****$p < 0.0001$) (Figure 1H). In a similar fashion, the TGFβ1-CTPR390 group resulted in an inhibition of the TGFβ1-dependent decline of the capacity of the ECCT to absorb elastic strain energy before yielding (resilience) (Figure 1I). These findings suggest that the TGFβ1-activated ECCT treated with CTPR390 (TGFβ1-CTPR390 group) exhibited elastic properties and a recovery capacity from deformation similar to those observed under control condition (Figure 1I).

CTPR390 reduces pro-fibrotic gene and protein expression in fibrotic ECCTs

Previous data from our group detailed the anti-fibrotic mechanism of action of the CTPR390, which inhibits Hsp90 by binding to its C-terminal end. This causes a conformational change in the Hsp90 dimer and displaces it from the TGFβ receptor complex, altering TGFβ signaling without toxicity when CTPR390 enters fibroblasts.[20,35] This activity reduced the expression of collagen and other pro-fibrotic markers.[20,25,26] Building on these findings, we demonstrated anti-fibrotic effects of CTPR390 in TGFβ1-activated ECCT. After administering CTPR390 to ECCTs with TGFβ1-activated fibroblasts, fluorescence from Alexa-488 confirmed the presence of CTPR390 throughout the tissue (Figures 2A and 2B). Further examination revealed CTPR390 inside human TGFβ1-activated fibroblasts (Figure 2C). An enzymatic digestion process was then employed to extract fibroblasts from the ECCT, followed by cultivation to re-confirm the presence of CTPR390 and assess cell survival in culture after 13 days within the ECCT (Figures 2D and 2E). Notably, a significant percentage of the total fibroblasts within the ECCT demonstrated internalization of CTPR390 (83.3% ± 7.0%) (Figure 2D). This incorporation did not induce toxicity in either fibroblasts or cardiomyocytes, as demonstrated by the comparable viability of cells treated and untreated with CTPR390 (Figure S2B). Furthermore, we confirmed that CTPR390 has a comparable ability to reduce COL I A1 and COL III A1 expression as commercial Hsp90 inhibitors, such as 17AAG and EGCG, in human

Figure 2. Restoration of Control ECCT gene and protein expression following the introduction of CTPR390 to TGFβ1-activated ECCT

(A) Bright-field and epifluorescence imaging of control representative images of ECCT, TGFβ1-activated ECCT, and TGFβ1-activated ECCT subjected to CTPR390 treatment (Control, TGFβ1 and TGFβ1-CTPR390). Both white scale bars in the two panels indicated 5 mm.

(B) Diagram illustrating the detection of CTPR390-green fluorescence (resulting from Alexa 488 fluorophore conjugated to CTPR390) incorporated into ECCT. It included a close-up view of the fluorescent fibroblasts within the ECCT and the subsequent extraction of fibroblasts from the ECCT, transferred to a tube, and later seeded onto a culture plate, revealing both fluorescent and non-fluorescent fibroblasts. Diagram generated with Biorender.

(C) CTPR390 fluorescence captured directly from the surface of the TGFβ1 ECCT following a 13-day treatment with CTPR390 (TGFβ1-CTPR390 group). The white scale bar indicated 10 μm.

(D) Bar graphs presenting the percentage and total cells retaining CTPR390 over a 13-day period in TGFβ1-CTPR390 ECCT, $n = 4$ ECCT per group, with three technical replicates.

(E) Visualization of bright-field, nuclei (Hoechst) and CTPR390 (Alexa 488), along with the merged representation of all three images, pertaining to purified fibroblasts derived from TGFβ1-CTPR390 group and cultured in 2D plates. The white scale bar indicated 50 μm.

(F) Heatmap illustrating the prevalent pro-fibrotic genes, with darker red representing higher expression (2x over the median) and light reds indicating lower expression (0.5 lower the median) in Control, TGFβ1, and TGFβ1-CTPR390 ECCT groups; n = 6–10 ECCT per group with 3 technical replicates of each ECCT sample.

(G and H) XY plots illustrating the comparison of expression for all pro-fibrotic genes tested between TGFβ1-CTPR390 and TGFβ1groups (G), as well as between TGFβ1 and Control groups (H).

(I) Bar graphs illustrating significant gene expression differences of the most differentially expressed pro-fibrotic genes tested in Control, TGFβ1 and TGFβ1-CTPR390 groups; n = 6–10 ECCT per group with 3 technical replicates of each ECCT sample. All datasets passed the Shapiro-Wilk test for normal distribution. p-values for all graphs (*$p < 0.05$, **$p < 0.005$, ***$p < 0.0005$, ****$p < 0.0001$) were determined using one-way ANOVA with Tukey's multiple comparison test.

(J) Representative confocal images depicting the localization of COL I A1, COL III A1, FN, and FAP proteins in cross-sections of ECCTs. A higher density of superficial cells (indicated by DAPI-stained nuclei), and COL IA1, was observed in TGFβ1-activated ECCT s compared to the Control and TGFβ1-CTPR390-treated groups. CTPR390 was visualized using Alexa 488 fluorescence. The white scar bars indicated 50 μm. In all graphs, error bars represent the variability of the data as standard deviation.

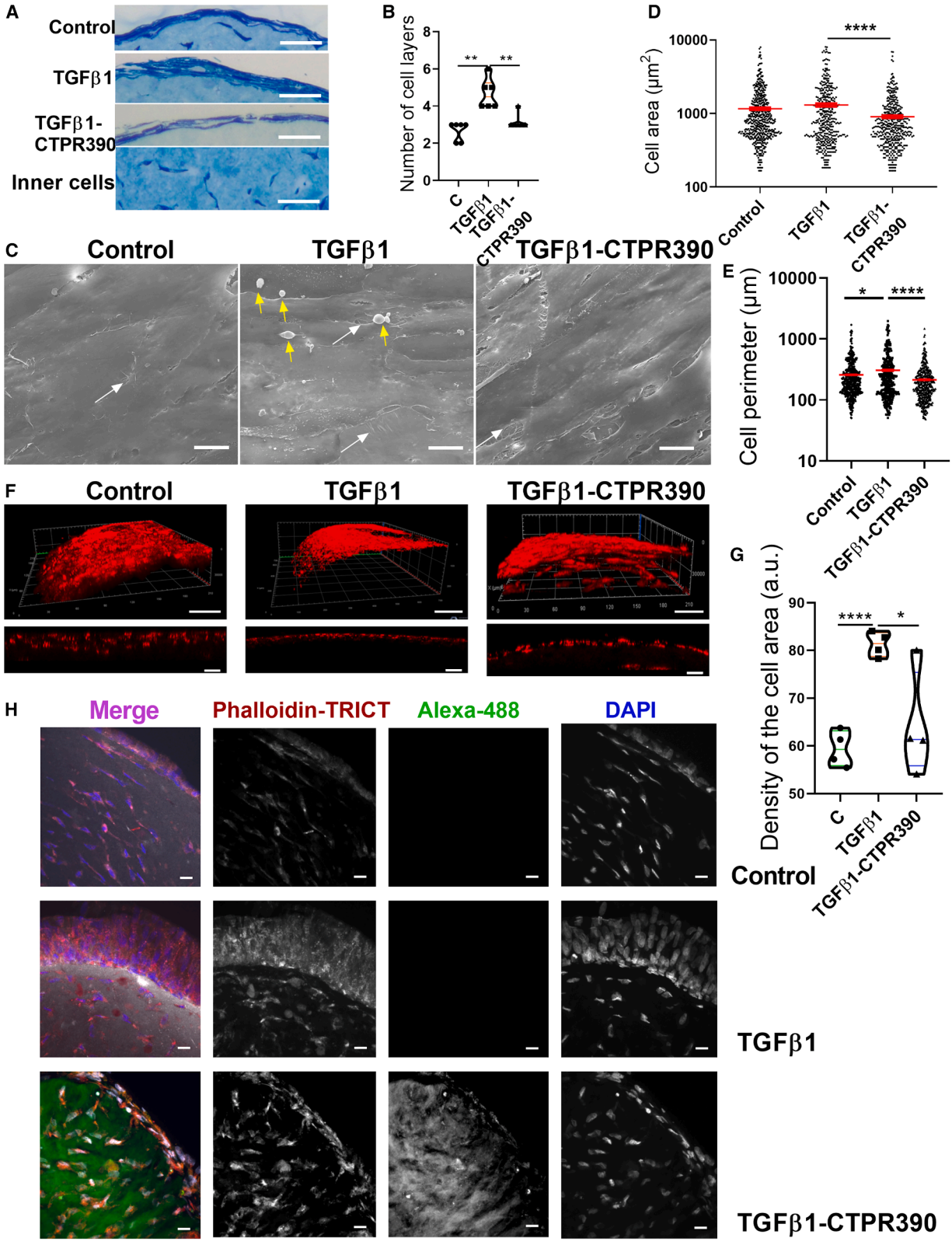

(legend on next page)

cardiac fibroblasts (Figure S2D). These findings highlighted the potential of CTPR390 as a promising molecule for further studies, moving closer to clinical translation.

In this study, the relative gene expression of previously reported myofibroblast and fibroblast markers, identified as differentially regulated in this human model at earlier time points,[17] was analyzed. The results, highlighting significant differences, are presented in a heatmap (Figure 2F). Two xy plots were used to identify the most differentially expressed genes by comparing the Control ECCT group with the TGFβ1 group and the TGFβ1 group with the TGFβ1-CTPR390 group (Figures 2G and 2H). It is noteworthy that crucial activated fibroblast markers, including COL I A1, COL III A1, PDGFRA, LOX and POSTN, showed a moderate to strong up-regulation in response to TGFβ1 (Figures 2F and 2G) and a down-regulation in response to CTPR390 (Figures 2F and 2H). We emphasized the potent anti-fibrotic effect of CTPR390 by demonstrating a significant reduction in the expression of critical pro-fibrotic genes, clearly showing differences in the gene expression of COL I A1, COL III A1, PDGFRA, LOX, and POSTN (Figure 2I). At the protein level, we observed a marked reduction in COL I A1 expression and a slight decrease in FAP in TGFβ1-CTPR390. In all cases, CTPR390 treatment reduced the number of superficial cells, along with key pro-fibrotic protein expression (COL I A1 and FAP) in these areas. No changes were detected in FN expression or COL III A1 (Figure 2J). Interestingly, the same human cardiac fibroblasts cultured in 2D showed no differences in COL I A1 and FAP protein expression between Control and TGFβ1-activated fibroblasts, except for COL III A1 (Figure S2E).

CTPR390 avoids the pro-fibrotic cell profile in TGFβ1-treated ECCT

In all groups (Control, TGFβ1, and TGFβ1-CTPR390), hematoxylin-eosin staining of cross-sections extracted from the medial region of the long branch of the ECCT revealed elongated superficial fibroblasts compared to inner cells (Figure 3A). Surface cells were aligned in the pole-to-pole direction, while interior cells were arranged randomly within the ECCT (Figure 3A). CTPR390 treatment significantly reduced the number of fibroblast layers on the surface of TGFβ1-activated ECCT, from 4.5 ± 0.5 layers to 2.5 ± 0.5 layers (**$p < 0.005$), bringing it closer to control levels (Figure 3B). Scanning electron microscopy showed higher surface activity in TGFβ1-activated ECCT, with more filopodia and blebs, indicating intense cell-matrix interactions and membrane stress. In contrast, Control and TGFβ1-CTPR390 ECCT s exhibited less cellular activity, with reduced filopodia presence (Figure 3C). The observed bleb formation in TGFβ1-activated fibroblasts of fibrotic ECCT is typically seen when the cell membrane detaches from the underlying actin cytoskeleton. This can occur due to increased internal pressure and mechanical stress, causing the membrane to balloon outward.[36] In contrast, Control and TGFβ1-CTPR390 ECCT showed less cellular activity, although CTPR390 treatment still maintained some active surface areas by showing reduced areas with filopodia (Figure 3C). Cell count analysis showed a reduction in cell area (Figure 3D) and cell perimeter (Figure 3E) in TGFβ1-CTPR390 ECCT s compared to TGFβ1-activated ones (Figures 3D and 3E). Fibroblasts from the ECCT, as happens in the heart,[37] appeared to be a key component for sustaining the tension of the tissue. To corroborate this, we used collagen without fibroblasts to form an ECCT (Figure S3A), which resulted in the formation of a diffused, not solidified ECCT unattached to the poles. However, the presence of fibroblasts resulted in a tense ECCT that was attached to the two poles and presented regular short and long arms (Figure S3B). Moreover, when collagen was deposited and solidified in culture media, it formed a dense, uniform layer from any angle of observation, indicating the absence of varying angles of polarization (AoP) (Figures S3C and S3D). Lysotracker labeling confirmed higher cell density on the surface of TGFβ1-activated ECCT compared to Control (****$p < 0.0001$) and TGFβ1-CTPR390 ECCT (*$p < 0.05$) (Figures 3F and 3G). The formation of actin stress fibers and their presence in the cytoplasm are indicative of active fibroblasts. Actin stress fibers are strongly induced in activated fibroblast populations under conditions of increased isometric tension or stimulation with TGFβ1, resulting in an enhanced capacity for contractile force generation.[38] The heightened activation state of fibroblasts in TGFβ1-activated ECCT was supported by

Figure 3. Attenuation of TGFβ1-activated ECCT pro-fibrotic cell features after CTPR390 treatment

(A) Representative images of ECCT surface with fibroblasts stained with hematoxylin-eosin from cross-sections of Control, TGFβ1 and TGFβ1-CTPR390 ECCTs and representative image of inner fibroblast from an ECCT; the white scale bars indicated 25 μm.

(B) Violin plots depicting significant differences in the number of cell surface layers of TGFβ1 ECCT compared to Control and TGFβ1-CTPR390 ECCT, $n = 6$ independent samples measured in triplicate.

(C) Three panels featuring a depiction with a front view of fibroblasts on the surface of Control, TGFβ1 and TGFβ1-CTPR390 ECCTs by scan microscopy of 1 ECCT per group. Yellow arrows indicate surface blebs, and white arrows indicate filopodia in Control, TGFβ1 and TGFβ1-CTPR390 ECCTs; the white scale bars indicated 6 μm.

(D and E) (D) Cell area count and, e) Cell perimeter count in the three groups of ECCT (Control, TGFβ1 and TGFβ1-CTPR390) performed in $n = 12$ ECCT per group, n of cells = 400–510 cells per group.

(F) Confocal images showcasing the 3D reconstruction of cellular surfaces within 100 μm depth utilizing lysotracker (in red) as a cell dye for comparing cell surface density in Control, TGFβ1, and TGFβ1-CTPR390 ECCTs. The white scale bars in upper panels indicated 30 μm and the white scale bars in lower panels indicated 40 μm.

(G) Violin graph presenting the analysis of significant differences in the density of cell area in Control, TGFβ1, and TGFβ1-CTPR390 ECCTs; $n = 4$ independent ECCT samples measured in triplicate. The dataset from (G) passed Shapiro-Wilk test for normal distribution. The p-values for (G) which followed a normal distribution (*$p < 0.05$, ****$p < 0.0001$), were determined using one-way ANOVA with Tukey's multiple comparison test. p-values for the dataset in (B), (D), and (E) (*$p < 0.05$, **$p < 0.005$, ****$p < 0.0001$) were determined using the non-parametric Mann-Whitney test, as the data did not follow a normal distribution.

(H) Representative confocal images of ECCT cross-sections visualizing human actin-F (phalloidin-TRICT staining), CTPR390 fluorescence (Alexa 488), and nuclei (DAPI staining) in the surface and inside areas of control, TGFβ1 and CTPR390 ECCT. The white scale bars indicated 10 μm. In all graphs, error bars represent the variability of the data as standard deviation.

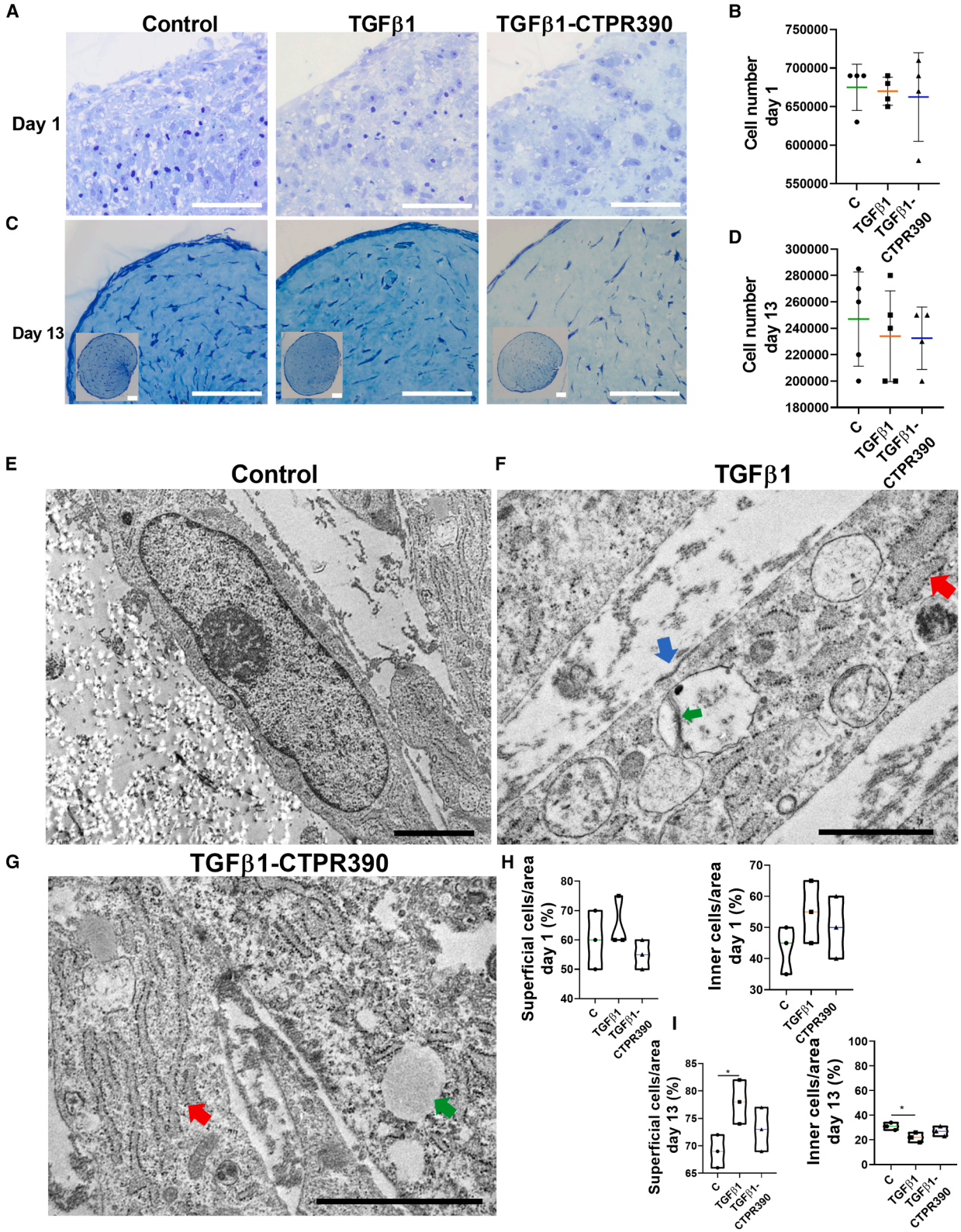

(legend on next page)

increased actin cytoskeleton abundance stained with phalloidin (Figure 3H). In contrast, TGFβ1-CTPR390 ECCT showed normal actin expression and reduced surface cell accumulation, as confirmed by nuclear DAPI staining (Figure 3H).

CTPR390 preserves fibroblast distribution and structure in fibrotic ECCT

At day 0, 750,000 human primary cardiac fibroblasts are embedded in the bovine collagen to generate the 3D engineered tissue; once the ECCT compacts on day 1, the model featured a media of 680,000 homogeneously distributed fibroblasts throughout the 3D tissue (Figures 4A and 4B). After 13 days of culture, the cell organization changed and exhibited a particular segregation with differential cell separation between the ECCT surface and the ECCT interior (Figure 4C), with a total cell number, presenting variations depending on the group: Control 247,000 ± 35,637; TGFβ1 234,000 ± 34,351; or TGFβ1-CTPR390 232,500 ± 23,629 (Figure 4D). A reduction in the initial cell number due to failed cell attachment regularly occurred during the maturation process of the ECCT.

The ultrastructure of the TGFβ1-activated ECCT (Figure 4F) revealed several differences compared to control fibroblasts (Figure 4E) such as an electron-dense depression of the plasma membrane (blue arrow), the engorged sacs of rough endoplasmic reticulum (RER) (red arrow) or the presence of vesicle containing very electron-dense fibrous elements (green arrow) (Figure 4F) indicating increased cellular activity. CTPR390 treatment (Figure 4G) resulted in normally shaped RER sacs (red arrow) comparable to the control (Figure 4E) and the presence of vacuoles (green arrow), which did not appear under Control or TGFβ1 conditions. Notably, ECCT inner fibroblasts exhibited a more rounded morphology compared to superficial fibroblasts (Figures S3E–S3G). We calculated the percentage of superficial fibroblasts relative to the total number of fibroblasts per area on day 1 and day 13. The results showed that the initial fibroblast distribution (day 1) was similar among groups and across the superficial and interior areas of the ECCT (Figure 4H). On day 13, the total distribution of fibroblasts changed, showing a higher percentage of superficial fibroblasts in the TGFβ1-activated ECCT compared to the Control group (Figure 4I), with a corresponding reduction in the percentage of inner fibroblasts compared to the Control group (Figure 4I). The TGFβ1-CTPR390 group showed no significant differences compared to either the Control or TGFβ1 groups.

CTPR390 diminished the production of structured collagen in fibrotic ECCT

Collagen deposition during tissue remodeling is regulated by local stresses and strains.[39] The ECCT activated with TGFβ1 simulates tissue remodeling influenced by these local stress forces, as illustrated in Figure 1. Scanning electron microscopy revealed a tubular structure with layers of fibroblasts encasing the ECM on the tissue surface across all groups (Control, TGFβ1 and TGFβ1-CTPR390) (Figure 5A). A detailed examination of the inner ECM in TGFβ1-activated ECCTs revealed structures resembling cellular debris, indicative of poorer cell accommodation (Figure 5B). Further analysis revealed a significant reduction of elastin gene and protein, confirming the higher stiffness of the tissue (Figures S4A and S4B). The TGFβ1 group displayed enhanced ECM activity, along with indicators of apoptosis and cell proliferation at both the gene and protein levels, which were not observed in the Control or TGFβ1-CTPR390 ECCTs (Figures S4C–S4H). Cross-sectional area (CSA) measurements of TGFβ1-activated ECCTs showed a significant reduction compared to Control ECCTs (****$p < 0.0001$) and TGFβ1-CTPR390 ECCTs (*$p < 0.05$) (Figure 5C). This reduction was attributed to matrix compaction by TGFβ1-activated fibroblasts. Fibrotic ECCTs treated with CTPR390 (TGFβ1-CTPR390 group) showed partial protection from this compaction (*$p < 0.05$), corroborated by perimeter measurements (Figure 5D). A significant correlation between CSA and perimeter was observed in Control ECCTs (****$p < 0.0001$) but disappeared with TGFβ1 treatment and was not restored by CTPR390 (Figure 5E). Collagen fibers, when organized in a more structured and aligned manner, exhibit birefringence or the ability of a material to refract light in two different directions. The birefringence given by the polarized light passing through structured collagen of ECCTs enabled us to distinguish between regions of the 3D engineered tissue characterized by organized collagen and those with less organized or unstructured collagen. The polarized light technique differentiated between structured and unstructured collagen based on light refraction.[40] The technique proved particularly valuable for distinguishing between structured collagen generated by human fibroblasts on the surface of the ECCT (light signal) and the unstructured collagen (dark areas),

Figure 4. Characterization of distinct fibroblast subtypes in the ECCT

(A and C) Hematoxylin/eosin staining on day 1 (A) and day 13 (C) of cross-sections of Control, TGFβ1, and TGFβ1-CTPR390 groups including insets of the whole cross section (C). The white bars of all panels indicated 50 μm, including inset panels showing the whole ECCTs.

(B and D) Quantification of total cell numbers on day 1 (B) and day 13 (D) of Control, TGFβ1, and TGFβ1-CTPR390 groups. Cell counts were performed in 3–5 biological samples per group including 3 technical replicates per sample.

(E–G) Electron microscopy images of superficial fibroblasts showing representative ultrastructural features of Control (E), TGFβ1 (F), and TGFβ1-CTPR390 (G) ECCT on day 13.

(F) The blue arrow marks a depression of the plasma membrane; the red arrow points to a sac of rough endoplasmic reticulum (RER); and the green arrow points to one of the vesicles with very electron-dense fibrous elements.

(G) The red arrow points to a normal-shaped RER sac; and the green arrow indicates a vacuole. Black scale bars indicated 2 μm (E, G) and 3 μm (F).

(H and I) Bar graphs showing the percentage of superficial and inner fibroblasts per area on day 1 (H) and day 13 (I); $n = 3$ biological samples per group in triplicate were measured. The p values (*$p < 0.05$) were determined using a one-way ANOVA with Tukey's multiple comparison test. All datasets, except for (B), passed the Shapiro-Wilk test for normal distribution. p-values for datasets following a normal distribution (*$p < 0.05$) were determined using one-way ANOVA with Tukey's multiple comparison test. The dataset for (B) did not show significant differences, and to assess significance, p-values were calculated using the non-parametric Mann-Whitney test, as the data did not follow a normal distribution. In all graphs, error bars represent the variability of the data as standard deviation.

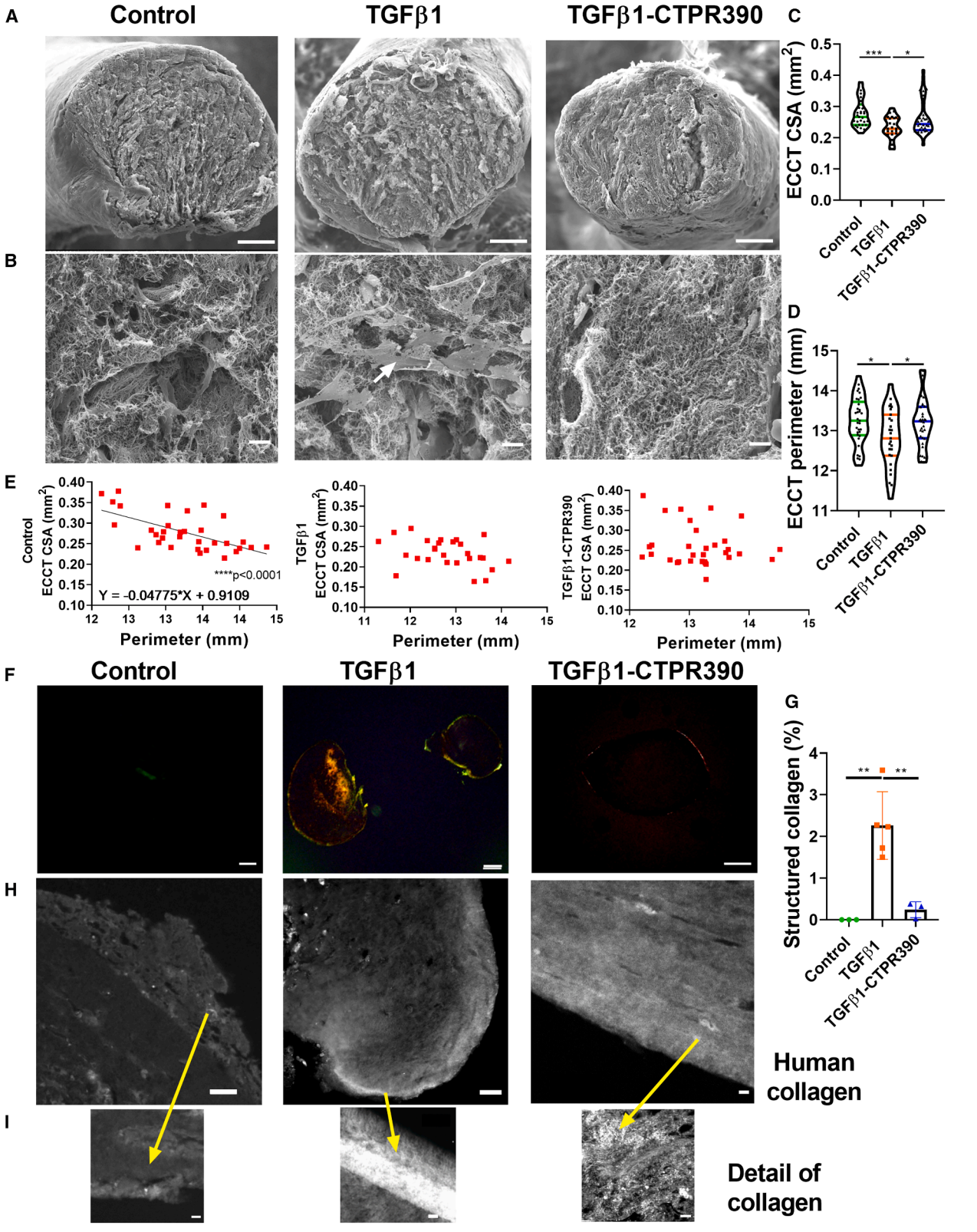

(legend on next page)

confirming the organized arrangement of collagen fibers in TGFβ1-activated tissues (Figure 5F). Quantification revealed significantly more structured collagen in TGFβ1-activated ECCTs compared to Control (**$p < 0.001$) or TGFβ1-CTPR390 ECCTs (**$p < 0.001$) (Figure 5G).

Recognizing that the human-derived ECM was predominantly localized on the surface of the ECCT, the study aimed to distinguish between the human ECM produced by human cardiac primary fibroblasts and the bovine collagen initially used to embed the cells within the 3D tissue. Thus, to differentiate human ECM from bovine collagen of the ECCT, we first tested the species specificity of the human collagen Ia1 antibody. It showed no signal in bovine collagen, but positive labeling in ECCT-surface collagen (Figure S4I). TGFβ1-activated ECCTs had a higher human collagen signal compared to Control and TGFβ1-CTPR390 ECCTs (Figure 5H), in a manner consistent with the marking by polarized light shown in Figure 5G. The multiphoton imaging technique utilizes nonlinear optical effects to visualize collagen structures in biological tissues. Specifically, it relies on two-photon excitation, where two photons of lower energy combine to excite a fluorophore. In the case of collagen, Second Harmonic Generation (SHG) is the predominant signal observed. Structured collagen, such as that found in organized and aligned fibers, produces a strong and specific SHG signal. This is because the nonlinear optical process is enhanced in highly ordered structures. As a result, multiphoton imaging can efficiently highlight regions with well-organized collagen arrangements. On the other hand, unstructured or less organized collagen, lacking a clear pattern or alignment, generates a weaker or absent SHG signal. Multiphoton microscopy can thus differentiate between areas of tissue where collagen is organized in a structured manner (signal detection) and regions where collagen is less organized or unstructured (no signal). This differentiation was essential for comprehending and verifying the return to a control-like state with non-organized collagen in TGFβ1-CTPR390 condition (Figure 5I), and for confirming the high organization achieved by human collagen within TGFβ1-activated ECCT (Figure 5I). The yellow arrow indicated the locations where magnifications were taken, revealing a clear greater thickness of human collagen in TGFβ1-activated ECCT compared to Control or TGFβ1-CTPR390 ECCT s (Figure 5I).

Fiber orientation preserved after CTPR390 treatment to fibrotic ECCT

Preferential angles and degree of fibers orientation (mainly collagen as shown in previous figures) were obtained from SAXS patterns and plotted as 2D maps (Figures 6A–6C). We analyzed the level of collagen organization within each of the ECCTs by analyzing the anisotropy of the scattering patterns (Figures 6 and S5).[41] The analysis conducted on each $20 \times 20\ \mu m^2$ pixel image of the ECCT surface revealed that the percentage of organized areas (those with a degree of orientation over 0.15) in the ECCT was similar between Control and fibrotic ECCT, with values of 91.7% in TGFβ1-activated ECCT and 92.3% in Control ECCT. However, a significant increase was observed in the organization level of fibers present in those extracellular matrix (ECM) areas in TGFβ1-activated ECCT compared to Control ECCT. This organization level was determined by the relative degree of orientation in TGFβ1-activated ECCT, which was 0.56 ± 0.25 versus 0.52 ± 0.22 in Control ECCT (Figure 6D). It is noteworthy that the fibers of TGFβ1-activated ECCT appeared to avoid these high levels of organization after treatment with CTPR390 (Figures 6C and 6D). The significant decrease in both the extent of organized ECCT areas and the degree of orientation of these areas in TGFβ1-CTPR390 ECCT was evident from the significantly lower values obtained for the percentage of structured area (80.9%) compared to TGFβ1-activated ECCT, as well as the organization level of those areas (0.42 ± 0.26), which is significantly lower (****$p < 0.0001$) than the value for TGFβ1-activated ECCT (0.56 ± 0.25) (Figures 6C and 6D).

DISCUSSION

In this study, we advanced preclinical human models to assess experimental drugs that had previously shown promising results

Figure 5. Localization of organized collagen produced by human fibroblasts on the surface of TGFβ1-activated ECCT

(A) Representative cross-sectional scanning microscopy images of Control, TGFβ1 and TGFβ1-CTPR390 long arms of the ECCTs. The white scale bars indicated 100 μm.

(B) Representative magnified scanning microscopy images of inner-sections of Control, TGFβ1 and TGFβ1-CTPR390 ECCTs. The white scale bars indicated 10 μm.

(C and D) Violin graph illustrating a significant reduction of the TGFβ1 ECCT cross section area (CSA in mm^2) (C), and a reduction of the TGFβ1 ECCT perimeter (in mm) (D), indicating a higher degree of compaction in TGFβ1 samples in comparison to Control or TGFβ1-CTPR390 ECCTs (n = 15–33 independent ECCTs analyzed per group with 3 technical replicates per sample).

(E) Positive and significant correlation (****$p < 0.0001$) between CSA and perimeter of Control ECCTs. The other two groups (TGFβ1, and TGFβ1-CTPR390) did not show a correlation between the CSA and their respective perimeters (n = 25–33 ECCTs analyzed per group with 3 technical replicates per sample).

(F) Representative images showing distinctively colored structured collagen at the periphery of the TGFβ1-activated ECCT (central panel) under polarized light. In contrast, there was very low detection of structured collagen in the other two groups under study. The white scale bars indicated 50 μm.

(G) Bar graph showing the percentage of structured collagen assessed through polarized light; n = 4–5 ECCT samples per group with 3 technical replicates per sample. All datasets, except for (C), passed the Shapiro-Wilk test for normal distribution. p-values for datasets following a normal distribution (*$p < 0.05$, **$p < 0.005$) were determined using one-way ANOVA with Tukey's multiple comparison test. For (C), where the dataset did not follow a normal distribution, p-values (*$p < 0.05$, ***$p < 0.0005$) were determined using the non-parametric Mann-Whitney test.

(H) Representative confocal imaging of the ECCT surface detecting human collagen (COL I A1 antibody) showed a clear increase in collagen detection in TGFβ1 samples compared to Control or TGFβ1-CTPR390 samples. The white scale bars indicated 10 μm.

(I) Second Harmonic Generation (SHG) signal showing the clear accumulation of collagen in TGFβ1 ECCTs compared to Control or TGFβ1-CTPR390 ECCTs. Yellow arrows indicated the place of the augmentation. The white scale bars indicated 5 μm, except the fifth panel that indicated 10 μm. In all graphs, error bars represent the variability of the data as standard deviation.

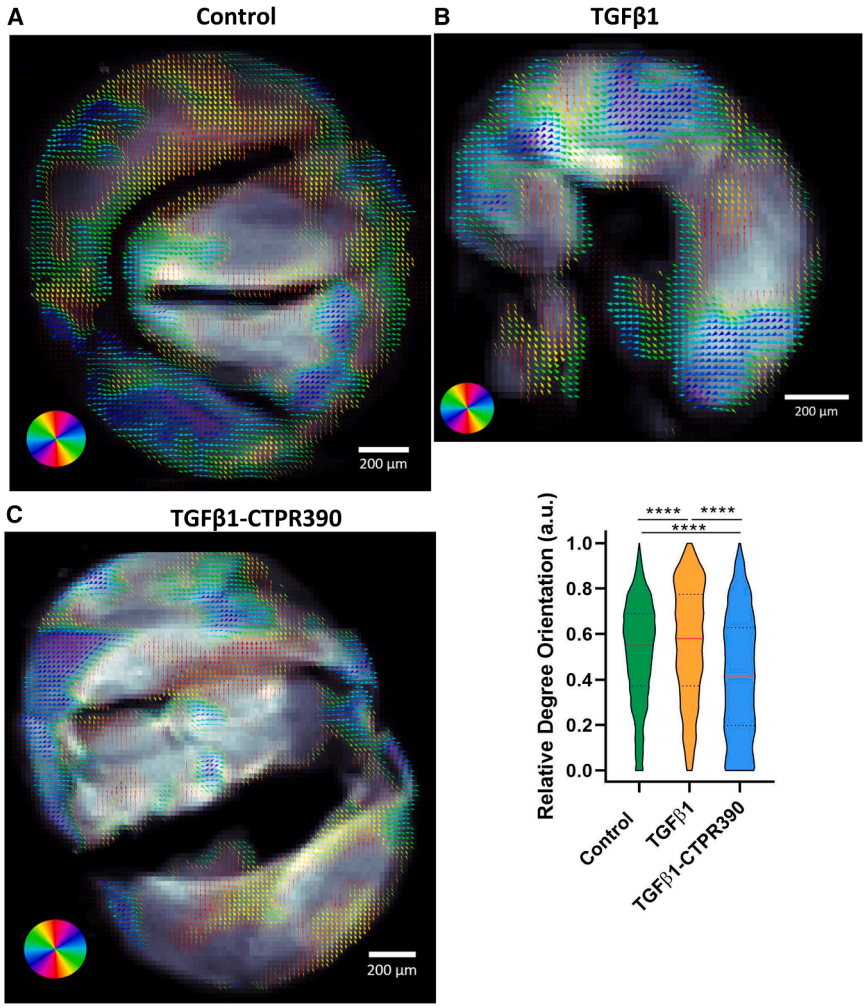

Figure 6. Differences in organization of collagen produced by human fibroblasts on the surface of TGFβ1-activated ECCT

(A–C) Maps of the preferential orientation and degree of orientation of collagen in control (A), TGFβ1(B), and TGFβ1-CTPR390 (C) ECCTs. The white scale bars indicated 200 μm. Preferential of orientation in each 20 × 20 μm^2 pixel is indicated by the direction of the arrow in each of the pixels of the figure and the color-coded discs. Degree of orientation in each 20 × 20 μm^2 pixel is indicated by the thickness of the arrows in each of the pixels of the figure. Maps from individual ECCTs are found expanded in Figures S5A–S5C.

(D) Violin graph illustrating significant changes in the degree of orientation of collagen in TGFβ1 (increase) and TGFβ1-CTPR390 (decrease) ECCTs. Graph was obtained considering the values from all of the pixels from each ECCT analyzing one complete ECCT per group including 3000–4000 pixels analyzed per ECCT. The dataset for panel (D) did not pass the Shapiro-Wilk test for normality. *p*-values (****$p < 0.0001$) were determined using the non-parametric Mann-Whitney test, as the data did not follow a normal distribution. $N = 5191$-2051 measurements of 1 ECCT per group. In all graphs, error bars represent the variability of the data as standard deviation.

in 2D cultures and *in vivo* models.[20,25] The specific action of CTPR390 in inhibiting TGFβ receptor I-Hsp90 binding instead of reducing its chaperone activity,[20,25] as commercial inhibitors do, presents an advanced mechanism of action which implies preserving the key chaperon function of Hsp90 thus cellular homeostasis. Moreover, the capacity in collagen reduction that was demonstrated here and in our previous studies,[20,25] comparable over the commercial Hsp90 inhibitors such as 17AAG implies an important advance in the future translation of CTPR390 to avoid the toxicity generated. The previously mentioned *in vivo* and 2D culture demonstrations of CTPR390 as an anti-fibrotic molecule settled the bases of this study that relies on Hsp90 inhibition in a 3D human cardiac model. Replicating the physical forces acting on the heart, including the ECM and fibroblasts, is crucial in a 3D model to capture their impact on morphology, biomechanics, and biochemical behavior. The adaptation used in this study accommodates such forces in both pathological and physiological scenarios, similar to approaches employed in other organs distinct from cardiac tissue.[42–44] The fibrotic ECCT model, which mimics human cardiac scar tissue, is a valuable tool to study drug behavior.[12] In our study, it helped identify the ultrastructural features associated with the anti-fibrotic treatment CTPR390. Our results showed that this treatment reduced pro-fibrotic markers in TGFβ1-activated human cardiac fibroblasts and altered fiber organization in the fibrotic ECCT, making it more similar to control ECCT. Previously, TGFβ1 activation induced pathological ECM changes that were reversed by CTPR390 in 2D cultures.[35] Moreover, the introduction of the hypertensive agent angiotensin II induced TGFβ1 activation, resulting in heart hypertrophy and fibrosis in a mouse model. This effect was successfully reversed through the administration of CTPR390.[20,25] Here, we show that CTPR390 restored biomechanical parameters in fibrotic ECCT, addressing TGFβ1-induced changes. The advantage of analyzing the effects of CTPR390 in the ECCT model, compared to the previously studied *in vivo* animal model, was to demonstrate in human cardiac fibroblasts results similar to those observed in preventing cardiac fibrosis in the *in vivo* mouse heart. It is important to highlight that in the ECCT system, human cardiac fibroblasts experience tissue-like tension forces in a 3D distribution, recreating a fibrotic area of the human heart. The detailed analysis of biomechanical, biochemical, and ultrastructural changes in human ECCT after CTPR390 treatment reinforces the protective effect against cardiac fibrosis observed in mice. We described the significance of TGFβ in triggering ECM fiber structuring and alignment in engineered human cardiac fibrotic tissue, which increases tissue stiffness and compaction. Importantly, CTPR390 demonstrated protection against this alignment, promoting a reversion to control conditions by reducing ECM-related gene expression. These

findings, which could not be suggested by previous *in vivo* studies, significantly enhance the translational relevance of our results.

Treated ECCTs had more variable fiber orientations and distributions, unlike the narrow alignment seen in fibrotic tissue. By segmenting fiber orientation, we detected alignment, providing other ways to study human cardiac fibrosis non-invasively. Tensile testing showed that CTPR390 prevented the increased stiffness of TGFβ1-activated ECCT, returning it to control levels. Contractility measurements confirmed that treated ECCTs exhibited biomechanical properties similar to controls. The biomechanical properties observed in TGFβ1-CTPR390 group were a direct outcome of its activity within fibroblasts. We demonstrated the penetration of the fluorescent CTPR390 into human fibroblasts within the tissue, showcasing its anti-fibrotic therapeutic properties. At the molecular level, these therapeutic capabilities, validated in 2D and *in vivo* models,[20,25,26] resulted in a reduction in the expression profile of cardiac fibrosis-associated genes in the human ECCT. CTPR390 prevented the overexpression of key pro-fibrotic markers, including COL I A1, COL III A1, LOX, PDGFRA, and POSTN. Unlike in 2D cultures, protein regulation in ECCT more accurately represented the pro- and anti-fibrotic effects of cardiac remodeling as it is the case for COL III, which has been implicated in altering the balance of collagen distribution during cardiac pathological remodeling to prevent cardiac dysfunction.[45]

TGFβ1 activation heightened ECM production and increased fibroblast concentration in superficial tissue regions. Fibrotic human fibroblasts displayed greater activity, including filopodia and bleb formation, increased cell elongation, and larger cell areas and perimeters. CTPR390 treatment mitigated these pathological changes, reducing superficial fibroblast density and collagen formation, while maintaining the number of viable cells and preventing ECM accumulation in fibrotic tissue. These actions maintained an ECCT architecture similar to control, thereby preventing the internal accumulation of additional ECM structures observed in fibrotic ECCTs.

TGFβ1-activated fibroblasts exhibited electron-dense depressions in the plasma membrane, indicating active trafficking, as well as engorged sacs of rough endoplasmic reticulum (RER), suggesting a high level of protein transcription activity, which was restored after CTPR390 treatment. Additionally, vesicles containing highly electron-dense fibrous elements were observed, possibly representing exocytotic vesicles transporting fibers to the ECM. Superficial fibroblasts in the TGFβ1-CTPR390 ECCT displayed vacuoles; however, these were not accompanied by any signs of stress or apoptosis, and the fibroblasts maintained their elongated shape, aligning with tissue force. No morphological differences were seen in fibroblasts within the tissue core, regardless of treatment. This suggests that the fibrotic tissue reorganized itself, recruiting activated cells to regions driving tissue remodeling, leaving other areas unaffected. These actions could resemble the connective tissue regions affected by remodeling and those not affected by such remodeling in the heart, where resident fibroblasts become active or remain in a quiescent state depending on the needs. Fibroblasts of TGFβ1-CTPR390 ECCTs also displayed a return of the endoplasmic reticulum to baseline thickness, indicating a reduction in pro-fibrotic protein production. These changes aligned with normal myocardial conditions, where fibroblasts maintain heart homeostasis by contributing to ECM that distributes mechanical forces.[46]

Our data demonstrated that ECCT fibroblasts responded to pathological stimuli, similar to heart fibroblasts during post-inflammatory cardiac remodeling.[47–50] This phenomenon is observed in all types of cardiac fibrosis, including perivascular fibrosis, reactive fibrosis, and replacement fibrosis.[51] Cross-sections of fibrotic ECCTs showed compaction and a less homogeneous ECM, which CTPR390 treatment prevented. In fibrotic areas, structured overexpressed collagen was observed, but CTPR390 reduced this to control levels. Additionally, CTPR390 treatment could not fully restore the correlation between compaction and perimeter values lost in fibrotic ECCTs, and subtle differences, like vacuoles, were found in TGFβ1-CTPR390 group. X-ray scattering patterns provided nanoscale data on collagen structured areas, revealing higher level of organization for collagen in fibrotic ECCTs and less organized areas with lower level of structuration in treated and control tissues. Collagen orientation was linked to tissue stiffness, supporting findings from PS-OCT. The structural characterization validated collagen's biomechanical properties across control, fibrotic, and anti-fibrotic ECCTs.

The significance of this work lies in the solid foundation established by a thorough *in vivo* investigation, which demonstrates the significant ability of CTPR390 to reduce fibrosis in the hearts of fibrotic mice.[20,25] Building on these results, this study provided precise data showcasing fibrosis reduction in a human model, shedding light on the dynamic interplay between the cardiac ECM and fibroblasts. Under applied tension forces, this interaction drives cellular reorganization and localization changes within the 3D human tissue, influencing cell morphology and collagen-enriched areas. In these regions, fibrotic pathology is associated with an increase in fiber orientation, which we observe and analyze in detail. Furthermore, this study provides insights for testing therapeutic drugs targeting cardiac conditions such as fibrosis. The 3D system we employed enabled comprehensive observations of tissue plasticity across multiple dimensions, capturing detailed data on cell ultrastructure, size, location, function, morphology, ECM organization, tissue compaction, biomechanical properties, dimensional changes, and the expression of pro-fibrotic biomarkers.

The use of ECCT as a model to analyze cardiac fibroblast responses to fibrosis and CTPR390-mediated fibrosis protection provides a solid foundation for understanding the synthesis and organization of ECM components. Focusing on specific regions of the myocardium with a high density of fibroblasts and their ECM production during pathological heart remodeling (ECCT model) offers an opportunity to demonstrate the effects of CTPR390 on cardiac fibroblasts within these specialized niches. To further demonstrate the efficacy of CTPR390 as an anti-fibrotic drug, it is essential to evaluate its effects in more complex models that better replicate areas of the tissue in which fibroblasts are in close contact with other major type of cardiac cells. A logical next step is to increase the complexity of the model by incorporating cardiomyocytes, or cardiomyocytes and stroma cells (EHM or EHT models) enabling fibroblasts to interact with them. These approaches (EHM or EHT models),

which more closely mimics cardiac environments focus on different cardiac cell types interaction, will be studied in the future to continue understanding the CTPR390 influences in different context representing cardiac fibrosis.

Our study offers a comprehensive characterization of fibrotic area orientation and ECM organization using advanced SAXS atomic technology. Here, we integrated a bench-to-clinic approach with PS-OCT to translate the detailed structural insights provided by SAXS into a clinically applicable imaging modality. Our findings demonstrate the restoration of biomechanical properties and tissue structure to a healthy state, alongside ultrastructural changes in fibroblasts within tension zones. This work highlights the limitations of traditional 2D models, emphasizing the superior accuracy of 3D tissue models that incorporate physical forces. These models more effectively capture the variations in pro-fibrotic markers and provide insights into preventing the progression of cardiac fibrotic regions, findings that are reported here.

In conclusion, our findings underscore the intricate relationship between ECM and fibroblasts in tissue biomechanics, offering insights for anti-fibrotic therapies and diagnosis.

The Table 1 provides specifications of each primer used in this study.

Limitations of the study

(1) The technical limitations of producing ECCT from a cell batch is a limitation to rule out any potential influence of sex on the observed outcomes.

(2) *In vivo* experiments were not included in the present work, as comprehensive *in vivo* studies evaluating the same therapeutic strategy have already been conducted and published by our group.[20,25] These prior findings provided evidence of efficacy and served as the rationale for advancing to the human-based engineered tissue models presented in this study. To maintain scientific integrity and avoid redundancy, the previously reported *in vivo* data were not replicated here. Instead, this manuscript focuses on translating those results into a human-relevant *in vitro* system, which offers complementary insights.

(3) Another limitation of this study is the absence of the "Control-CTPR390" group under certain experimental conditions. As outlined in the main text, this decision was based on our previously published data[20] and other tests, which showed comparable cell viability and pro-fibrotic gene expression between the Control-CTPR390 and the Control group (Figures S2B and S2C). Nonetheless, the lack of this control may influence the interpretation of specific results. Future studies will incorporate this group to support more rigorous comparative analyses.

RESOURCE AVAILABILITY

Lead contact

Requests for further information should be directed to and will be fulfilled by the lead contact Ana V Villar villarav@unican.es.

Materials availability

This study did not generate unique reagents. All materials used in this study will be made freely available upon request and the completion of applicable material transfer agreements. The information about reagents or other materials are provided in the key resources table.

Data and code availability

- **Data:** Data have been deposited at our institutional repository "https://unican-my.sharepoint.com". Data reported in this paper will be shared by the lead contact upon request.
- **Code:** This paper does not report original code.
- **Additional information:** Any additional information required to reanalyze the data reported in this paper is available from the lead contact upon request.

ACKNOWLEDGMENTS

This work was partially supported by Agencia Estatal de Investigación (AEI/MCI/10.13039/501100011033), Spain. A.V.V. PID2021-125702OB-I00. Fomento de la transferencia de conocimiento en la Comunidad Autónoma de Cantabria SUBVTC-2023-0006 T. A.L.C. acknowledges support by the Agencia Estatal de Investigación Grant PDC2021-120957-I00-NanoIVD and PDC2022-133345-I00-ProIMAGE funded by MCIN/AEI/10.13039/501100011033 and by the "European Union NextGenerationEU/PRTR" and Grant PID2022-137977OB-I00-ProTher funded by MCIN/AEI/ 10.13039/501100011033. C.S.C. thanks Gipuzkoa Foru Aldundia (Gipuzkoa Fellows program) Grant number 2019-FELL-000018-01/62/2019 for financial support. G. G. thanks the financial support of "la Caixa" Foundation (ID100010434, fellowship: LCF/BQ/DI20/11780020). This work was performed under the Maria de Maeztu Units of Excellence and Severo Ochoa Centers Programs from the Spanish State Research Agency – Grants No. MDM-2017-0720 (CIC biomaGUNE) and CEX2018-000867-S (DIPC). O.M.C. and V.M. thank the AEI for the infrastructure EQC 2019-006589-P and the PREVAL 21/07 grant from IDIVAL. We thank Dr. Ilan Davis for his supportive and conceptual contribution to the manuscript. We acknowledge DESY (Hamburg, Germany), a member of the Helmholtz Association HGF, for the provision of experimental facilities. Parts of this research were carried out at PETRA III P62 SAXSMAT beamline. Beamtime was allocated for proposals I-20210691 EC and I-20220193 EC.

AUTHOR CONTRIBUTIONS

Conceptualization, A.L.C., S.L., O.M.C., C.S.-C., and A.V.V.; methodology, D. M.L., A.N.D., A.P., H.S., J.M.I., G.G., V.M., A.L.C.C., and I.L.; formal analysis, D.M.L., G.H.d.O., H.S., V.M., A.V.V., and A.L.C.; investigation: protein hybrid synthesis and characterization and analytical studies, G.G., investigation: *in vitro* and *in vivo* studies, D.M.L., A.P., and A.V.V.; investigation: PS-OCT analysis, V.M. and O.M.C.; writing – original draft preparation, D.M.L., G.G., V.M., O.M.C., C.S.C., A.L.C., S.L., C.S.C., and A.V.V.; funding acquisition, A. L.C., C.S.C., and A.V.V. All the authors have read and agreed to the published version of the manuscript.

DECLARATION OF INTERESTS

There are no conflicts to declare.

STAR★METHODS

Detailed methods are provided in the online version of this paper and include the following:

- KEY RESOURCES TABLE
- EXPERIMENTAL MODEL AND STUDY PARTICIPANT DETAILS
  - Cell culture measurements of primary human cardiac fibroblasts
  - Differentiation of human induced pluripotent stem cells (hiPSCs) into cardiomyocytes
- METHOD DETAILS
  - Preparation of human engineered cardiac connective tissue
  - ProtCTPR390 expression and purification
  - Conjugation of CTPR390-AuNC with Alexa Fluor 488
  - CTPR390 fluorescence

Table 1. Primer table

Name	Sequence	Amp size	Annealing Temperature	Accession numbers	Additional hits or unintended alignments
COL Ia1	Fw:CCAGCAGATCGAGAACATCC Rv:CAGAGTGGCACATCTTGAGG	47 bp	55°C	XM_005257058	No
COL IIIa1	Fw:GACCAAAAGGTGATGCTGGC Rv:ACCGTTAGCTCCTGGTTTCC	161bp	53°C	NM_000090	No
LOX I	Fw:CAAGGGACATCAGATTTCTTACC Rv:CCATACTGTGGTAATGTTGATGAC	82bp	53°C	NM_001178102	No
PDGFRA	Fw:GCTCTTTACTCCATGTGTGGGA Rv:ATTAGGCTCAGCCCTGTGAGA	127bp	55°C	NM_006206	No
TCF21	Fw:AACGACAAATACGAGAACGGGT Rv:CTCCAGGTACCAAACTCCAAGG	154bp	54°C	NM_198392	No
FAP	Fw:GCTTTGAAAAATATCCAGCTGCC Rv:ACCACCATACACTTGAATTAGCA	141bp	54°C	XM_011510796	No
FN	Fw:ACAACACCGAGGTGACTGAGAC Rv:GGACACAACGATGGTTCCTGAG	143bp	56°C	NM_212476	No
ACTA2	Fw:AGAACATGGCATCATCACCA Rv:GCGTCCAGAGGCATAGAGAG	229bp	52°C	NM_001406462	No
POSNT	Fw:CCCTTGGAAGAGACGGTCAC Rv:CTCAAAGACTGCTCCTCCCA	182bp	55°C	NM_001330517	No
Elastin	Fw:TTCCCCGCAGTTACCTTTCC Rv:CTAAGCCACCAACTCCTGGG	121bp	56°C	NM_001278918	No
Ki67	Fw:ATTTGCTTCTGGCCTTCCCC Rv:CCAAACAAGCAGGTGCTGAG	164bp	55°C	NM_002417	No
CCND1	Fw:CTGATTGGACAGGCATGGGT Rv:GTGCCTGGAAGTCAACGGTA	322bp	55°C	NM_053056	No
FGF2	Fw:CCCCAGAAAACCCGAGCGA Rv:TTCACGGATGGGTGTCTCCG	226bp	58°C	NM_002006	No
PDGFRB	Fw:CAGCTCTGGCCCTCAAAGG Rv:GAACGAAGGTGCTGGAGACA	132bp	55°C	NM_001355017	No
BAX	Fw:AGGGGCCCTTTTGCTTCAG Rv:TGTCCAGCCCATGATGGTTC	355bp	56°C	NM_004324	No
BCL2	Fw:GAAGGTTTCCTCGTCCCTGG Rv:GAAGACCCTGAAGGACAGCC	248bp	56°C	NM_000633	No
P53	Fw:AGTCTAGAGCCACCGTCCAG Rv:TCCGGGGACAGCATCAAATC	276bp	56°C	NM_001407269	No
CTGF	Fw:GAGAGTCCTTCCAGAGCAGC Rv:CATAGTTGGGTCTGGGCCAA	245bp	55°C	NM_001901	No
P21	Fw:AGTCAGTTCCTTGTGGAGCC Rv: CATTAGCGCATCACAGTCGC	291bp	55°C	NM_001374513	No
GREM1	Fw:TAAGCAGACCATCCACGAGG Rv:GGCAGTTGAGTGTGACCATC	179bp	54°C	NM_001191323	No
FSP1	Fw:CCCTGGATGTGATGGTGTCC Rv:CGATGCAGGACAGGAAGACA	225bp	55°C	NM_002961	No
HSP90AA1	Fw:GGTCCTGTGCGGTCACTTAG Rv:TATCTGCACCAGCCTGCAAA	407bp	55°C	NM_005348	No
HSP90AB1	Fw:AACCGCCCTGCTATCTTCTG Rv:ACAAACTCCTTGCCACACCA	124bp	54°C	NC_000006.12	No
GAPDH housekeeping gene	Fw:TGCACCACCAACTGCTTAGC Rv:GGCATGGACTGTGGTCATGAG	87 bp	56°C	NM_002046	No

Description of the primer sequences expected amplicon sizes (bp), annealing temperatures (°C), and GenBank accession numbers. Amplicon sizes and specificity were verified using NCBI Primer-BLAST, and annealing temperatures were calculated using the NEB Tm Calculator. The housekeeping gene used is indicated. Primers were designed and validated using NCBI's Primer-BLAST tool, with the reference sequences identified by their respective accession numbers. Specificity was confirmed using the "Search for primer pair specificity" option in Primer-BLAST against the RefSeq mRNA database (organism: Homo sapiens). Primers were considered specific when no additional hits or unintended alignments were detected beyond the target gene.

- ECCT compaction analysis by cross-sectional area measurement
- Stress-strain analysis of destructive tensile strength measurements
- Enzymatic digestion of ECCT to disaggregate fibroblasts
- Fluorescence live cell and ECCT imaging
- Polarization-sensitive optical coherence tomography
- Immunochemistry of ECCT: TUNEL assays
- *In vitro* treatment of ECCT with TGFβ1 and CTPR390
- Quantitative PCR analysis of cell samples
- Confocal fluorescence microscopy of ECCT cross-sections
- Transmission electron microscopy
- Scanning electron microscopy
- Cellular area, perimeter and layers quantification
- Cell viability and counting method
- Assessment of Hsp90 inhibitors in human cardiac fibroblasts
- Polarized light imaging of picrosirius red staining samples
- Multiphoton microscopy
- SAXS imaging

- QUANTIFICATION AND STATISTICAL ANALYSIS

SUPPLEMENTAL INFORMATION

Supplemental information can be found online at https://doi.org/10.1016/j.isci.2025.113013.

Received: December 12, 2024
Revised: March 21, 2025
Accepted: June 24, 2025
Published: June 26, 2025

REFERENCES

1. Frangogiannis, N.G. (2021). Cardiac fibrosis. Cardiovasc. Res. *117*, 1450–1488.
2. Villalobos Lizardi, J.C., Baranger, J., Nguyen, M.B., Asnacios, A., Malik, A., Lumens, J., Mertens, L., Friedberg, M.K., Simmons, C.A., Pernot, M., and Villemain, O. (2022). A guide for assessment of myocardial stiffness in health and disease. Nat. Cardiovasc. Res. *1*, 8–22.
3. Van Norman, G.A. (2017). Overcoming the Declining Trends in Innovation and Investment in Cardiovascular Therapeutics: Beyond EROOM's Law. JACC. Basic Transl. Sci. *2*, 613–625.
4. Hofbauer, P., Jahnel, S.M., and Mendjan, S. (2021). In vitro models of the human heart. Development *148*, 23.
5. Inoko, M., Kihara, Y., Morii, I., Fujiwara, H., and Sasayama, S. (1994). Transition from compensatory hypertrophy to dilated, failing left ventricles in Dahl salt-sensitive rats. Am. J. Physiol. *267*, H2471–H2482.
6. Klotz, S., Hay, I., Dickstein, M.L., Yi, G.H., Wang, J., Maurer, M.S., Kass, D.A., and Burkhoff, D. (2006). Single-beat estimation of end-diastolic pressure-volume relationship: a novel method with potential for noninvasive application. Am. J. Physiol. Heart Circ. Physiol. *291*, H403–H412.
7. Mirsky, I., Pfeffer, J.M., Pfeffer, M.A., and Braunwald, E. (1983). The contractile state as the major determinant in the evolution of left ventricular dysfunction in the spontaneously hypertensive rat. Circ. Res. *53*, 767–778.
8. Tiburcy, M., Meyer, T., Satin, P.L., and Zimmermann, W.H. (2022). Defined Engineered Human Myocardium for Disease Modeling, Drug Screening, and Heart Repair. Methods Mol. Biol. *2485*, 213.
9. Bremner, S., Goldstein, A.J., Higashi, T., and Sniadecki, N.J. (2022). Engineered Heart Tissues for Contractile, Structural, and Transcriptional Assessment of Human Pluripotent Stem Cell-Derived Cardiomyocytes in a Three-Dimensional, Auxotonic Environment. Methods Mol. Biol. *2266*, 2261–2262.
10. Krause, J., Lemme, M., Mannhardt, I., Eder, A., Ulmer, B., Eschenhagen, T., and Stenzig, J. (2022). Human-Engineered Atrial Tissue for Studying Atrial Fibrillation. Methods Mol. Biol. *2211*, 2261–2262.
11. Kittana, N., Assali, M., Zimmermann, W.H., Liaw, N., Santos, G.L., Rehman, A., and Lutz, S. (2021). Modulating the Biomechanical Properties of Engineered Connective Tissues by Chitosan-Coated Multiwall Carbon Nanotubes. Int. J. Nanomedicine *16*, 989–1000.
12. Santos, G.L., Meyer, T., Tiburcy, M., DeGrave, A., Zimmermann, W.H., and Lutz, S. (2021). Fibroblast Derived Human Engineered Connective Tissue for Screening Applications. J. Vis. Exp. *20*, 62700.
13. Meyer, F.E.U., Santos, G.L., Doan, T.P., DeGrave, A.N., Bues, B., and Lutz, S. (2023). Pirfenidone affects human cardiac fibroblast proliferation and cell cycle activity in 2D cultures and engineered connective tissues. Naunyn-Schmiedebergs Arch Pharmacol *396*, 1687–1699.
14. Cadosch, N., Gil-Cruz, C., Perez-Shibayama, C., and Ludewig, B. (2024). Cardiac Fibroblastic Niches in Homeostasis and Inflammation. Circ. Res. *134*, 1703–1717.
15. Voorhees, A.P., and Han, H.C. (2014). A model to determine the effect of collagen fiber alignment on heart function post myocardial infarction. Theor. Biol. Med. Model. *11*, 6–4682.
16. Yokota, T., McCourt, J., Ma, F., Ren, S., Li, S., Kim, T.H., Kurmangaliyev, Y.Z., Nasiri, R., Ahadian, S., Nguyen, T., et al. (2020). Type V Collagen in Scar Tissue Regulates the Size of Scar after Heart Injury. Cell *182*, 545–562.e23.
17. Santos, G.L., DeGrave, A.N., Rehman, A., Al Disi, S., Xhaxho, K., Schröder, H., Bao, G., Meyer, T., Tiburcy, M., Dworatzek, E., et al. (2022). Using different geometries to modulate the cardiac fibroblast phenotype and the biomechanical properties of engineered connective tissues. Biomater. Adv. *139*, 213041.
18. Chaudhury, A., and Howe, P.H. (2009). The tale of transforming growth factor-beta (TGFbeta) signaling: a soigné enigma. IUBMB Life *61*, 929–939.
19. Burgos Villar, K.N., Liu, X., and Small, E.M. (2022). Transcriptional regulation of cardiac fibroblast phenotypic plasticity. Curr. Opin. Physiol. *28*, 100556.
20. Caceres, R.A., Chavez, T., Maestro, D., Palanca, A.R., Bolado, P., Madrazo, F., Aires, A., Cortajarena, A.L., and Villar, A.V. (2018). Reduction of cardiac TGFbeta-mediated profibrotic events by inhibition of Hsp90 with engineered protein. J. Mol. Cell. Cardiol. *123*, 75–87.
21. Frangogiannis, N.G. (2020). Transforming growth factor-β in tissue fibrosis. J. Exp. Med. *217*, 2.
22. Ficker, E., Dennis, A.T., Wang, L., and Brown, A.M. (2003). Role of the cytosolic chaperones Hsp70 and Hsp90 in maturation of the cardiac potassium channel HERG. Circ. Res. *92*, e87–e100.
23. Ohkubo, S., Kodama, Y., Muraoka, H., Hitotsumachi, H., Yoshimura, C., Kitade, M., Hashimoto, A., Ito, K., Gomori, A., Takahashi, K., et al. (2015). TAS-116, a highly selective inhibitor of heat shock protein 90α and β, demonstrates potent antitumor activity and minimal ocular toxicity in preclinical models. Mol. Cancer Ther. *14*, 14–22.
24. Serwetnyk, M.A., and Blagg, B.S.J. (2021). The disruption of protein-protein interactions with co-chaperones and client substrates as a strategy towards Hsp90 inhibition. Acta Pharm. Sin. B *11*, 1446–1468.
25. Aires, A., Maestro, D., Ruiz Del Rio, J., Palanca, A.R., Lopez-Martinez, E., Llarena, I., Geraki, K., Sanchez-Cano, C., Villar, A.V., and Cortajarena, A.L. (2020). Engineering multifunctional metal/protein hybrid nanomaterials as tools for therapeutic intervention and high-sensitivity detection. Chem. Sci. *12*, 2480–2487.
26. RuizdelRio, J., Guedes, G., Novillo, D., Lecue, E., Palanca, A., Cortajarena, A.L., and Villar, A.V. (2024). Fibroblast-derived extracellular vesicles as trackable efficient transporters of an experimental nanodrug with fibrotic heart and lung targeting. Theranostics *14*, 176–202.
27. Carrigan, P.E., Sikkink, L.A., Smith, D.F., and Ramirez-Alvarado, M. (2006). Domain:domain interactions within Hop, the Hsp70/Hsp90 organizing protein, are required for protein stability and structure. Protein Sci. *15*, 522–532.

28. Aires, A., Sousaraei, A., Möller, M., Cabanillas-Gonzalez, J., and Cortajarena, A.L. (2021). Boosting the Photoluminescent Properties of Protein-Stabilized Gold Nanoclusters through Protein Engineering. Nano Lett. *21*, 9347–9353.
29. Beloqui, A., and Cortajarena, A.L. (2020). Protein-based functional hybrid bionanomaterials by bottom-up approaches. Curr. Opin. Struct. Biol. *63*, 74–81.
30. Uribe, K.B., Guisasola, E., Aires, A., López-Martínez, E., Guedes, G., Sasselli, I.R., and Cortajarena, A.L. (2021). Engineered Repeat Protein Hybrids: The New Horizon for Biologic Medicines and Diagnostic Tools. Acc. Chem. Res. *54*, 4166–4177.
31. Cortajarena, A.L., Wang, J., and Regan, L. (2010). Crystal structure of a designed tetratricopeptide repeat module in complex with its peptide ligand. FEBS J. *277*, 1058–1066.
32. Cortajarena, A.L., Kajander, T., Pan, W., Cocco, M.J., and Regan, L. (2004). Protein design to understand peptide ligand recognition by tetratricopeptide repeat proteins. Protein Eng. Des. Sel. *17*, 399–409.
33. Cortajarena, A.L., Yi, F., and Regan, L. (2008). Designed TPR modules as novel anticancer agents. ACS Chem. Biol. *3*, 161–166.
34. RuizdelRio, J., Muñoz, P., Carreira, P., Maestro, D., Pablos, J.L., Palanca, A., Merino, J., Serrano-Mollar, A., Merino, R., Tamayo, E., et al. (2022). Profibrotic Role of Inducible Heat Shock Protein 90α Isoform in Systemic Sclerosis. J. Immunol. *209*, 38–48.
35. Groen, J., Palanca, A., Aires, A., Conesa, J.J., Maestro, D., Rehbein, S., Harkiolaki, M., Villar, A.V., Cortajarena, A.L., and Pereiro, E. (2021). Correlative 3D cryo X-ray imaging reveals intracellular location and effect of designed antifibrotic protein-nanomaterial hybrids. Chem. Sci. *12*, 15090–15103.
36. Fujii, Y., and Ikenouchi, J. (2024). Cytoplasmic zoning in membrane blebs. J. Biochem. *175*, 133–140.
37. Camelliti, P., Borg, T.K., and Kohl, P. (2005). Structural and functional characterisation of cardiac fibroblasts. Cardiovasc. Res. *65*, 40–51.
38. Sandbo, N., and Dulin, N. (2011). Actin cytoskeleton in myofibroblast differentiation: ultrastructure defining form and driving function. Transl. Res. *158*, 181–196.
39. Miller, A.D., and Tyagi, S.C. (2002). Mutation in collagen gene induces cardiomyopathy in transgenic mice. J. Cell. Biochem. *85*, 259–267.
40. Ryan, N., Shefelbine, S.J., and Shapiro, F. (2023). Automated measurement of lamellar thickness in human bone using polarized light microscopy. MethodsX *11*, 102428.
41. Conceição, A.L.C., Müller, V., Burandt, E.C., Mohme, M., Nielsen, L.C., Liebi, M., and Haas, S. (2024). Unveiling breast cancer metastasis through an advanced X-ray imaging approach. Sci. Rep. *14*, 1448.
42. Abdel Fattah, A.R., Kolaitis, N., Van Daele, K., Daza, B., Rustandi, A.G., and Ranga, A. (2023). Targeted mechanical stimulation via magnetic nanoparticles guides in vitro tissue development. Nat. Commun. *14*, 5281–41037.
43. Vian, A., Pochitaloff, M., Yen, S.T., Kim, S., Pollock, J., Liu, Y., Sletten, E. M., and Campàs, O. (2023). In situ quantification of osmotic pressure within living embryonic tissues. Nat. Commun. *14*, 7023–42024.
44. Xia, M., Wu, M., Li, Y., Liu, Y., Jia, G., Lou, Y., Ma, J., Gao, Q., Xie, M., Chen, Y., et al. (2023). Varying mechanical forces drive sensory epithelium formation. Sci. Adv. *9*, eadf2664.
45. Uchinaka, A., Yoshida, M., Tanaka, K., Hamada, Y., Mori, S., Maeno, Y., Miyagawa, S., Sawa, Y., Nagata, K., Yamamoto, H., and Kawaguchi, N. (2018). Overexpression of collagen type III in injured myocardium prevents cardiac systolic dysfunction by changing the balance of collagen distribution. J. Thorac. Cardiovasc. Surg. *156*, 217–226.e3.
46. Travers, J.G., Kamal, F.A., Robbins, J., Yutzey, K.E., and Blaxall, B.C. (2016). Cardiac Fibrosis: The Fibroblast Awakens. Circ. Res. *118*, 1021–1040.
47. Ali, S.R., Ranjbarvaziri, S., Talkhabi, M., Zhao, P., Subat, A., Hojjat, A., Kamran, P., Müller, A.M.S., Volz, K.S., Tang, Z., et al. (2014). Developmental heterogeneity of cardiac fibroblasts does not predict pathological proliferation and activation. Circ. Res. *115*, 625–635.
48. Fredj, S., Bescond, J., Louault, C., and Potreau, D. (2005). Interactions between cardiac cells enhance cardiomyocyte hypertrophy and increase fibroblast proliferation. J. Cell. Physiol. *202*, 891–899.
49. Moore-Morris, T., Guimarães-Camboa, N., Banerjee, I., Zambon, A.C., Kisseleva, T., Velayoudon, A., Stallcup, W.B., Gu, Y., Dalton, N.D., Cedenilla, M., et al. (2014). Resident fibroblast lineages mediate pressure overload-induced cardiac fibrosis. J. Clin. Investig. *124*, 2921–2934.
50. Teekakirikul, P., Eminaga, S., Toka, O., Alcalai, R., Wang, L., Wakimoto, H., Nayor, M., Konno, T., Gorham, J.M., Wolf, C.M., et al. (2010). Cardiac fibrosis in mice with hypertrophic cardiomyopathy is mediated by non-myocyte proliferation and requires Tgf-β. J. Clin. Investig. *120*, 3520–3529.
51. Thomas, T.P., and Grisanti, L.A. (2020). The Dynamic Interplay Between Cardiac Inflammation and Fibrosis. Front. Physiol. *11*, 529075.
52. Burridge, P.W., Matsa, E., Shukla, P., Lin, Z.C., Churko, J.M., Ebert, A.D., Lan, F., Diecke, S., Huber, B., Mordwinkin, N.M., et al. (2014). Chemically defined generation of human cardiomyocytes. Nat. Methods *11*, 855–860.
53. Santos, G.L., Hartmann, S., Zimmermann, W.H., Ridley, A., and Lutz, S. (2019). Inhibition of Rho-associated kinases suppresses cardiac myofibroblast function in engineered connective and heart muscle tissues. J. Mol. Cell. Cardiol. *134*, 13–28.
54. Schindelin, J., Arganda-Carreras, I., Frise, E., Kaynig, V., Longair, M., Pietzsch, T., Preibisch, S., Rueden, C., Saalfeld, S., Schmid, B., et al. (2012). Fiji: an open-source platform for biological-image analysis. Nat. Methods *9*, 676–682.
55. Haas, S., Sun, X., Conceição, A.L.C., Horbach, J., and Pfeffer, S. (2023). The new small-angle X-ray scattering beamline for materials research at PETRA III: SAXSMAT beamline P62. J. Synchrotron Radiat. *30*, 1156–1167.

STAR★METHODS

KEY RESOURCES TABLE

REAGENT or RESOURCE	SOURCE	IDENTIFIER
Antibodies		
FAP antibody	ThermoFisher	PA5-51057
COL I A1 antibody	Abcam	ab34710
COL III A1 antibody	Abcam	ab184993
αSMA antibody	Merck	A5228
Ki67 MIB-1 antibody	Algilent	Dako M7240
Elastin antibody	Santa Cruz Biotechnology	sc-374638
Bacterial and virus strains		
Escherichia coli strain	Prof. Aitziber L. Cortajarena Laboratory, CIC biomaGUNE	C41 (DE3)
Chemicals, peptides, and recombinant proteins		
TWEEN® 20	Merck	P1379
Triton X-100	Biorad	1610407
PFA 16%	ThermoFisher	28908
DAPI and Hoechst Nucleic Acid Stains	ThermoFisher	62248
mTeSR™1 medium	STEMCELL Technologies	Ref. 85850
Collagen type I	Collagen solutions LLC	Lot 9433
L-ascorbic acid 2-phosphate	Merck	A92902-25G
IPTG	Apollo Scientific	Ref BIMB1008
DMEM, powder, high glucose content	ThermoFisher	52100039
HumanKine® recombinant human TGF beta 1 protein	Proteintech	HZ-1011
CHIR99021	Medchemexpress	HY-10182
Wnt-C59	Medchemexpress	S7037
Oryza sativa-derived recombinant human albumin	Sigma-Aldrich/Merck	A0237
Plasmid encoding CTPR8(C390-C416His-E2C)	Dr. Aitziber L. Cortajarena Laboratory, CIC biomaGUNE	C390-C416His-E2C
StemPro™ Accutase™	ThermoFisher	A1110501
Colagenase	Merck	C0130-100MG
TRIzol® reagent	NZYtech	MB18503
TEV protease	Prof. Aitziber L. Cortajarena Laboratory, CIC biomaGUNE	N/A
Critical commercial assays		
In Situ Cell Death Detection Kit	Merck	12156792910
HisTrap Q column	Cytiva	17528601
myrPlates myriaMed	Myriamed	50-0105-0001
BioTek Synergy H1	Agilent	N/A
HisTrap Q column	Cytiva	17528601
Stereoscope	Zeiss	Lumar.V12
Rheometer	RSA-G2	TA Instruments
TEL221-PS	Thorlabs Inc.	N/A
CASY Ton	CASY OLS	5651808
P62 SAXSMAT beamline	PETRA III, Hamburg, Germany	N/A
Deposited data		
Raw and analyzed data	This paper	Institutional repository: unican-my.sharepoint.com

(*Continued on next page*)

Continued

REAGENT or RESOURCE	SOURCE	IDENTIFIER
Experimental models: Cell lines		
Human cardiac fibroblasts	Promocell	Lot 437Z012.4
hiPSCs	EBiSC	UKKi011-A
Oligonucleotides		
COL Ia1 Fw:CCAGCAGATCGAGAACATCC Rv:CAGAGTGGCACATCTTGAGG	This paper	accession code XM_005257058
COL IIIa1 Fw:GACCAAAAGGTGATGCTGGC Rv:ACCGTTAGCTCCTGGTTTCC	This paper	accession code NM_000090
LOX I Fw:CAAGGGACATCAGATTTCTTACC Rv:CCATACTGTGGTAATGTTGATGAC	This paper	accession code NM_001178102
PDGFRA Fw:GCTCTTTACTCCATGTGTGGGA Rv:ATTAGGCTCAGCCCTGTGAGA	This paper	accession code NM_006206
TCF21 Fw:AACGACAAATACGAGAACGGGT Rv:CTCCAGGTACCAAACTCCAAGG	This paper	accession code NM_198392
FAP Fw:GCTTTGAAAAATATCCAGCTGCC Rv:ACCACCATACACTTGAATTAGCA	This paper	accession code XM_011510796
FN Fw:ACAACACCGAGGTGACTGAGAC Rv:GGACACAACGATGGTTCCTGAG	This paper	accession code NM_212476
ACTA2 Fw:AGAACATGGCATCATCACCA Rv:GCGTCCAGAGGCATAGAGAG	This paper	accession code NM_001406462
POSNT Fw:CCCTTGGAAGAGACGGTCAC Rv:CTCAAAGACTGCTCCTCCCA	This paper	accession code NM_001330517
Elastin Fw:TTCCCCGCAGTTACCTTTCC Rv:CTAAGCCACCAACTCCTGGG	This paper	accession code NM_001278918
Ki67 Fw:ATTTGCTTCTGGCCTTCCCC Rv:CCAAACAAGCAGGTGCTGAG	This paper	accession code NM_002417
CCND1 Fw:CTGATTGGACAGGCATGGGT Rv:GTGCCTGGAAGTCAACGGTA	This paper	accession code NM_053056
FGF2 Fw:CCCCAGAAAACCCGAGCGA Rv:TTCACGGATGGGTGTCTCCG	This paper	accession code NM_002006
PDGFRB Fw:CAGCTCTGGCCCTCAAAGG Rv:GAACGAAGGTGCTGGAGACA	This paper	accession code NM_001355017
BAX Fw:AGGGGCCCTTTTGCTTCAG Rv:TGTCCAGCCCATGATGGTTC	This paper	accession code NM_004324
BCL2 Fw:GAAGGTTTCCTCGTCCCTGG Rv:GAAGACCCTGAAGGACAGCC	This paper	accession code NM_000633
P53 Fw:AGTCTAGAGCCACCGTCCAG Rv:TCCGGGGACAGCATCAAATC	This paper	accession code NM_001407269
CTGF Fw:GAGAGTCCTTCCAGAGCAGC Rv:CATAGTTGGGTCTGGGCCAA	This paper	accession code NM_001901
P21 Fw:AGTCAGTTCCTTGTGGAGCC Rv: CATTAGCGCATCACAGTCGC	This paper	accession code NM_001374513
GREM1 Fw:TAAGCAGACCATCCACGAGG Rv:GGCAGTTGAGTGTGACCATC	This paper	accession code NM_001191323
FSP1 Fw:CCCTGGATGTGATGGTGTCC Rv:CGATGCAGGACAGGAAGACA	This paper	accession code NM_002961
HSP90AA1 Fw:GGTCCTGTGCGGTCACTTAG Rv:TATCTGCACCAGCCTGCAAA	This paper	accession code NM_005348
HSP90AB1 Fw:AACCGCCCTGCTATCTTCTG Rv:ACAAACTCCTTGCCACACCA	This paper	accession code NC_000006.12
GAPDH housekeeping gene Fw:TGCACCACCAACTGCTTAGC Rv:GGCATGGACTGTGGTCATGAG	This paper	accession code NM_002046

(*Continued on next page*)

Continued

REAGENT or RESOURCE	SOURCE	IDENTIFIER
Software and algorithms		
ImageJ software	NIH	1.54n99
Python 3.8	Open source	NA
GraphPad Prism	GraphPad Software (Dotmatics)	v8, RRID: SCR_002798
Fiji	Open source (https://fiji.sc)	ImageJ 1.54i
Gatan	Gatan Inc.	NA

EXPERIMENTAL MODEL AND STUDY PARTICIPANT DETAILS

Cell culture measurements of primary human cardiac fibroblasts

We purchased adult human left ventricular cardiac fibroblasts from a male Caucasian donor through Promocell (Lot 437Z012.4). The authentication used for this cell line was positive qPCR assays of key markers (COL IA1, POSNT, PDGRFA, PDGRFB) included in Table 1 and included in the KRT. The cells were cultivated as a monolayer at 37°C under 5% CO_2 in humidified incubators, using FGM-3 growth medium (PromoCell) supplemented with 10% Fetal Calf Serum, Basic Fibroblast Growth Factor 1 ng/mL and Insulin 5 μg/mL, without adding antibiotics, following the manufacturer's guidelines. This cell line was tested for mycoplasma contamination, and the results were negative.

Differentiation of human induced pluripotent stem cells (hiPSCs) into cardiomyocytes

The widely established protocol[52] was employed to differentiate induced pluripotent stem cells (hiPSCs) (ID: UKKi011-A; EBiSC) into cardiomyocytes. The authentication used for this cell line was positive qPCR assays of key markers (SOX2, CNMD, NANOG), available upon request. Cells were maintained in mTeSR™1 medium (STEMCELL Technologies, ref. 85850) on geltrex-coated plates, with medium changes every two days and high confluency during seeding. To initiate differentiation, hiPSCs were seeded at a 1:10 ratio in new 6-well plates, achieving approximately 85% confluency after 4 days. On Day 0, the medium was switched to CDM3, prepared with RPMI 1640 medium (Life Technologies, ref. 11875), supplemented with 500 μg/mL Oryza sativa-derived recombinant human albumin (Sigma-Aldrich/Merck, ref: A0237), 213 μg/mL L-ascorbic acid 2-phosphate (Merck, ref: A92902-25G), and 6 μM CHIR99021 (Medchemexpress, ref: HY-10182, dissolved in 10 mM DMSO) for 48 h to activate the Wnt signaling pathway by inhibiting GSK-3. On Day 2, the medium was replaced with fresh CDM3 containing 2 μM Wnt-C59 (Medchemexpress, ref: S7037, dissolved in 10 mM DMSO) to inhibit Wnt signaling and promote cardiomyocyte differentiation. From Day 4 onwards, the cardiomyocytes were maintained in CDM3 base, with medium changes every two days. This cell line was tested for mycoplasma contamination, and the results were negative.

METHOD DETAILS

Preparation of human engineered cardiac connective tissue

The adult human left ventricular cardiac fibroblasts were expanded, and assayed for ECCT production were conducted between passages 3–4. The ECCT generation was performed as described before.[12] In brief, all required materials were pre-chilled, and all following steps were performed on ice. First, 0.3 mg/ECCT bovine collagen type I (Collagen solutions LLC) was mixed with 2 × DMEM and neutralized with 0.2 M NaOH. Then, resuspended 7.5×10^5 human cardiac fibroblast per ECCT in FGM-3 media were added and thoroughly mixed. The final volume per ECCT was 180 μL. The cell-collagen mixture was pipetted in 48-well mold plates containing two flexible poles containing a specific material named TM5MED (shore value A46, bending stiffness 1.5 mN/mm) (myrPlates myriaMed)[17,53] and let condensate for 1 h at 37°C in a cell incubator. The ECCT were cultured for 13 days, and the medium, including the additives, was changed every second day. The concentration of TGFβ1 used in this study (5 ng/mL) was consistent with the one previously employed in this model to induce fibrosis.[16] The optimal anti-fibrotic concentration of CTPR390 was previously established to be 1 μM based on the extrapolation of titration assays conducted in primary fibroblasts.[20]

ProtCTPR390 expression and purification

CTPR8(C390-C416His-E2C) (ProtCTPR390) was designed as a multifunctional protein scaffold. The chimera protein includes several modules: a wildtype module with the glutamate residue at position 2 (E2) mutated to cysteine to allow fluorophore conjugation through the highly selective and straightforward thiol-maleimide chemistry; a CTPR390 module for Hsp90 binding functionality, and a CTPR416His-E2C module with four tandem repeated CTPR units containing histidines at positions 2, 5, 9, and 13 of each repeat, serving as a metal coordination domain to stabilize the formation of AuNC. This module presents an additional point mutation to insert a single Cysteine for conjugation of selected fluorescence dyes (E2C). The plasmid encoding the CTPR8(C390-C416His-E2C) gene (ProtCTPR390) was transformed into Escherichia coli C41 (DE3). The protein of interest was expressed by culturing the bacteria under agitation at 37°C, and induced by the addition of 1 mM isopropyl β-*d*-thiogalactoside (IPTG) when they reached

an optical density of 0.6. Then, the cultures were grown overnight at 20°C. Cells were pelleted and resuspended in 50 mM Tris, 500 mM NaCl, pH 8.0. The cells were lysed through freeze-thaw cycles and lysed by sonication and centrifuged for 1 h at 10000 rpm. The overexpressed His-tagged CTPR390 protein was purified by affinity chromatography using a 5 mL HisTrap Q column (GE Healthcare). The His6-tag was then cleaved by Tobacco Etch Virus (TEV) protease overnight at room temperature, and then purified by size-exclusion chromatography. The protein concentration was determined by measuring the absorbance at 280 nm, using extinction coefficient calculated from the amino acid composition. Purity and size of the protein were confirmed by sodium dodecyl sulfate - acrylamide electrophoresis gel (SDS-PAGE), and by Matrix-Assisted Laser Desorption/Ionization-Time of Flight (MALDI-TOF) using an Applied Biosystems Voyager Elite MALDI-TOF mass spectrometer with delayed extraction (Applied Biosystems, Framingham, MA, USA). The protein secondary structure was verified by circular dichroism using a Jasco J-815 (JASCO Corporation, Tokyo, Japan). CD spectra were obtained at 2.5 μM of protein using a cuvette with 1 mm path length.

Synthesis of protein-stabilized gold nanoclusters (CTPRAu)

AuNC were stabilized on ProtCTPR390 protein through biomineralization, by optimizing a protocol previously described before.[28,53] Initially the protein buffer was changed to 150 mM of NaCl, 50 mM phosphate buffer at pH 10 using a PD-10 desalting column. Then, 1 mL of protein at 40 μM was incubated with 80 equivalents of Au per protein (21.4 μL of HAuCl4 at 150 mM) at 50°C for 30 min. Then, the protein was placed for 10 min on ice, followed by the addition of 8000 equivalents (213 μL at 1.5 M) of sodium ascorbate and incubation at 50°C for 72 h. After the synthesis, CTPR390-NC complex was centrifuged at 16,400 rpm for 1 h and subsequently concentrated using an Amicon filter with pore size of 10 kDa. Finally, the protein-nanomaterial hybrid was purified using a PD-10 desalting column and the buffer changed to PBS for further storage and use.[28]

Conjugation of CTPR390-AuNC with Alexa Fluor 488

After the synthesis of CTPR390-AuNC, the cysteine in the protein scaffold was conjugated with Maleimide C5 Alexa Fluor 488 (Thermo Fischer). For this, CTPR390-AuNC in PBS pH 7.4 were incubated with 10 equivalents of dithiothreitol (DTT) for 30 min at 4°C. Afterward, the DTT was removed using a PD-10 column and CTPR390-AuNC incubated with 13 equivalents of Maleimide C5 Alexa Fluor 488. The reaction was incubated for 4 h at 25°C. After the conjugation reaction the solution was concentrated, and the excess of dye removed using a PD-10 desalting column. All the samples were sterilized using a 0.22 μm syringe filter under sterile environment and stored in the fridge until further use. The protein concentration in the CTPR390-AuNC and CTPR390-AuNC-488 samples was determined by Pierce BCA Protein Assay Kits (Thermo Scientific) using as calibration line the same protein scaffold used for the synthesis of the hybrid nanomaterials (CTPR390). The amount of gold was determined by inductively coupled plasma mass spectrometry (ICP-MS, iCAP-Q ICP-MS, Thermo Scientific, Bremen, Germany) of samples previously digested with aqua regia. In summary, the CTPR390 used in this study contained its characteristic Hsp90 binding module fused to a histidine-based gold coordination domain and was mutated with a single cysteine for the conjugation with maleimide-Alexa 488 fluorophore. This protein was subsequently used to stabilize the formation of gold nanocluster (CTPR390-AuNC) and conjugated with Alexa 488 (CTPR390-AuNC-488).

CTPR390 fluorescence

The ProtCTPR390, CTPR390-AuNC, and CTPR390-AuNC-488 (CTPR390-AuNC-488 is named as CTPR390 in the main text) fluorescence was evaluated using a BioTek Synergy H1 hybrid microplate reader in a black 384-well plate. The fluorescence spectrum was recorded in RFU (Relative Fluorescence Units) against wavelength (nm) plots through a monochromator (1 s of integration time), measuring by the top, reading height of 7 mm, and gain of 100. The emission spectra were obtained by exciting the sample at 460 nm and recording the emission from 500 to 800 nm, or exciting the sample at 360 nm and recording the emission from 400 to 800 nm with a step of 2 nm.

ECCT compaction analysis by cross-sectional area measurement

Tissue compaction, which starts after collagen gelation, involves cell-driven matrix compression and remodeling. This is measured by the cross-sectional area (CSA) and volume of the tissues. On day 13, tissues were transferred to a DPBS multi-well plate, and top and side view images of the engineered cardiac tissues (ECCTs) were captured using a Lumar.V12 stereomicroscope.

Tissue diameters were analyzed at a minimum of 8 positions per imaging plane using ImageJ. Mean diameters from top (dt) and side (ds) views were calculated, and CSA was determined using the equation: $CSA = \pi \times (dt/2) \times (ds/2)$. The volume was calculated by multiplying the averaged CSA by the full length, measured from the top view using ImageJ.

Stress-strain analysis of destructive tensile strength measurements

To evaluate the mechanical properties of ECCT, destructive tensile strength measurements were performed using an RSA-G2 rheometer. ECCT samples were mounted on custom hooks, produced via 3D printing in-house, in a 37°C organ bath filled with DPBS and stretched uniaxially at a constant rate until rupture. ECCTs were stretched at 0.03 mm/s. Force values were divided by cross-sectional area (CSA) to obtain stress values, which were then plotted against the gap between hooks. The stress-strain curves were analyzed to identify the toe region, elastic region, and plastic region.

To calculate the given parameters (Young's modulus, strain to failure point) from the destructive tensile strength measurements, the measured force values (mN) were divided by the determined CSA (mm^2) to obtain stress values (kPa) and these were plotted

against the gap in mm (distance between the upper and lower hook) in GraphPad Prism. The obtained curves typically displayed the following regions: An initial region in which only background stress was measured, a short toe region, an elastic region in which the stress versus gap values were linear, a flattened plastic region, and finally a region of failure which was characterized by a sudden drop in stress due to the rupture of the tissues. To calculate the strain values, the beginning of the toe region was identified, and the corresponding gap length was considered as L0. The strain equation (Ltotal-L0)/L0 was used to transform the gap values, and the stress values at the beginning of the toe region were used for background subtraction. The slope of the elastic region was determined by linear regression and is presented in this work as Young's modulus. The strain to failure point, characterized by the sudden drop in stress, was identified manually. Due to the material-dependent variations in the absolute values, we compared only conditions which had been tested in parallel. Maximum stress, ultimate strain, and resilience were calculated using area under the curve (AUC) analysis. All assays were performed with $n = 12$ ECCT per group.

ECCT pole deflection were imaged daily over a 13-day period using a Nikon D90 camera with a Nikon AF-S NIKKOR 18-105mm lens. UVA light was used to enhance the visibility of the poles, allowing for precise measurement of their distance on the plate under sterile conditions. This setup ensured non-invasive, high-resolution imaging throughout the experiment. Images were analyzed with ImageJ software to measure the distance between the poles, which indicated the degree of pole defletion. Changes in pole distance was quantified relative to the initial measurement on day zero, providing a reliable measure of tissue biomechanical forces over the 13 days.

Enzymatic digestion of ECCT to disaggregate fibroblasts

For each experimental condition (Control, TGFβ1, TGFβ1-CTPR390, $n = 5$), ECCT organoids were digested using a two-step enzymatic process. Initially, organoids were treated with a 2 mg/mL Collagenase I solution for 3 h at 37°C. This was followed by a 30-min incubation with Accutase (detachment solution of proteolytic and collagenolytic enzymes) at 37°C. After each treatment, the resulting solution was collected and kept on ice. DPBS with 5% FBS was added to inactivate the enzymes. The combined cell solution was then centrifuged, and the cell pellet resuspended in culture medium. The cells were subsequently used for viability assays, cell counting, or prepared for microscopic observation.

Fluorescence live cell and ECCT imaging

On day 13, control ECCT group, TGFβ1-activated ECCT (TGFβ1) group, and TGFβ1-activated ECCT and treated with CTPR390 (TGFβ1-CTPR390) group were assessed for fluorescence. Excitation and emission were set at 488 nm and 495 nm, respectively to detect Alexa 488 fluorophore conjugated to CTPR390, Nikon Eclipse Ti2 microscope was employed.

On day 13, the human left ventricular cardiac fibroblasts embedded in ECCT were dissociated by incubating them in 2 mg/mL collagenase I in calcium-containing PBS in the presence of 20% FCS for 2 h at 37°C. Subsequently, the tissues were washed with PBS and further incubated in Accutase (Millipore), 0.0125% Trypsin, and 20 μg/mL DNAse (Calbiochem) for 30 min at 37°C. The cells were mechanically separated, and the enzymatic activity was halted by transferring them into PBS containing 5% FBS. After centrifugation for 10 min at 100 g and 4°C, the cells were resuspended in FGM-3 growth medium (Lonza) supplemented with 10% Fetal Bovine Serum (FBS, Gibco), 100 U/mL penicillin, and 100 μg/mL streptomycin (Gibco). The cells were either added to PBS containing 5% FBS and counted using a CASY TT system (Roche), or they were seeded in 35mm microscopy dishes (Ibidi μ-Dish 35 mm high Glass Bottom 81158) and incubated for 2 h at 37°C under 5% CO_2 in a humidified incubator. After washing, the medium was replaced with Leibovitz microscopy medium (Gibco 21083027). Inverted transmitted-light microscope, Primovert 491206-0001-000 Zeiss was used for the *in vivo* ECCT confocal images. Fluorescence belonging to the CTPR390 incorporated to the fresh TGFβ1-ECCT was detected with Orca flash 4 as a camera. A 60× oil objective with an opening of 1.4 mm was used. To detect CTPR390 –Alexa 488 fluorophore, excitation and emission were set at 488 nm and 495 nm, respectively. Objective 4×/Plan-Achromat 4x/0.10 for Primo Objective 10×/Plan-Achromat 10×/0.25 for Primo. Nikon Eclipse Ti2 was employed for 2D cell live image acquisition.

Polarization-sensitive optical coherence tomography

Polarization-sensitive optical coherence tomography distinguishes itself as a method with significant potential for offering a comprehensive depiction of the morphological architecture of tissues. Samples were measured with the TEL221-PS commercial system (Thorlabs Inc.), with 13 μm/pixel lateral and 5.5/n μm/pixel depth resolution. For the purpose of this work, $n = 1.38$ was used as the refractive index of all samples. Samples were imaged in a single sweep in approximately one minute each. The system illuminates the sample with circularly polarized light to excite all orientations of the sample's fibers equally. Afterward, the parallel ($\langle E_x^2 \rangle$) and perpendicular ($\langle E_y^2 \rangle$) components of the electric field are captured, and the Stokes parameters ($\vec{s} = (I, Q, U, V)$) are calculated ($I = \langle E_x^2 \rangle + \langle E_y^2 \rangle, Q = \langle E_x^2 \rangle - \langle E_y^2 \rangle, U = 2\langle E_x E_y \, cos(\delta) \rangle, V = 2\langle E_x E_y \, sin(\delta) \rangle$) at all points of the three-dimensional PS-OCT cube. The angle of polarization is then calculated as $AoP = 1/2 \; arctan \; (U/Q)$. To find the attenuation coefficient (μ_z), the Beer-Lambert law was applied to fit the PS-OCT signals to $I = I_{z=0} e^{-2\mu_z z}$, where $I_{z=0}$ represents the intensity (Stokes I) at the surface of the sample. The surface profile was obtained as the maximum intensity along depth for each xy position ($max(I(x,y,z)|_z)$). Kernel Density Estimation (KDE) was used to find the 2D distributions of the samples in the U-μ_z plane. The distributions were then bound to their 1 σ areas to find the overlap between samples by discretizing the space with a uniform 100 x 100 grid. Total areas analyzed excluded poles

contact area previously described as intrinsic fibrotic areas.[17] This measurements corresponded to the evolution along the depth (z) of the xy-averaged Stokes parameter (U) that characterized differences in tissue organization. The steady rate of change along depth (0–100 μm) corresponding to a linear relationship between U and z indicates some level of fiber uniformity (overall change below - 10% for all samples), with steeper slopes being markers of higher fiber alignment between different layers of the sample.

Immunochemistry of ECCT: TUNEL assays

ECCT previously fixed in PFD 4% and embedded in paraffin were permeabilized 30 min with 0.05% Triton X- in PBS. Immunochemical detection was carried out by incubating overnight at 4°C with the following anti human antibodies: anti-FAP antibody (1:100 dilution, PA5-51057), anti COL I A1 antibody (1:100 dilution, ab34710), anti COL III A1 antibody (1:100 dilution, ab184993), Anti-Fibronectin antibody (1:100 dilution, ab23750), anti-elastin-FITC (1:1000 dilution, A-8: sc-374638). The samples were washed with 0.05% Tween 20 in PBS, incubated for 1 h at room temperature with a secondary antibody (anti-human Cy5), washed in PBS. Fixated ECCT were left in PBS at 4°C for the subsequent confocal imaging. The same protocol was followed for the apoptosis assays using *In Situ* Cell Death Detection Kit (12156792910), TMR red. Terminal deoxynucleotidyl transferase-mediated TMR dUTP nick-end labeling (TUNEL) staining. An *in situ* cell death detection kit (Roche Diagnostics, Penzberg, Germany) was employed to detect apoptotic cells. ECCT vibratome sections (100 μm) were rinsed in PBS (3 × 10 min) and permeabilized at room temperature for 30 min with 0.5% Triton X-100 diluted in PBS. ECCT sections were incubated at 37°C with the TUNEL reaction mixture containing TMR-conjugated dUTP, terminal deoxynucleotidyl transferase and nucleotide mixture for 1h in a wet chamber. The samples were then washed with PBS and mounted with antifading solution. TUNEL staining was also combined with DAPI, mounted with vectashield and confocal images were processed with ImageJ.

In vitro treatment of ECCT with TGFβ1 and CTPR390

Once ECCT were generated using a mixture of collagen and adult human left ventricular cardiac fibroblasts, the Control group was incubated at 37°C with 5% CO_2. After 24 h, proper compaction to the poles was achieved. At this stage, the TGFβ1 group was treated with a final concentration of 5 ng/mL of TGFβ1, while the TGFβ1-CTPR390 group received 5 ng/mL of TGFβ1 along with 1 μM of CTPR390. To maintain these conditions, fresh media is replenished every four days, with the TGFβ1 group receiving fresh TGFβ1 (5 ng/mL) and the TGFβ1-CTPR390 group receiving fresh TGFβ1 (5 ng/mL) and fresh CTPR390 (1 μM).

Quantitative PCR analysis of cell samples

The total RNA from fibroblasts embedded into ECCT was obtained with TRIzol reagent (Gibco BRL, Grand Island, NY). Complementary DNA was prepared from 0.5 μg total RNA by random priming using a first-strand cDNA synthesis kit (Promega Corp). Primers sequence for the human genes using Sybr green QPCR were the following: COL I A1 forward: CCAGCAGATCGAGAACATCC; reverse: CAGAGTGGCACATCTTGAGG. COL III A1 forward: GACCAAAAGGTGATGCTGGC; reverse: ACCGTTAGCTCCTGGTT TCC. LOX I forward: CAAGGGACATCAGATTTCTTACC; reverse: CCATACTGTGGTAATGTTGATGAC. CTGF forward: GAGAGTC CTTCCAGAGCAGC; reverse: CATAGTTGGGTCTGGGCCAA. PDGFRA forward: GCTCTTTACTCCATGTGTGGGA; reverse: ATT AGGCTCAGCCCTGTGAGA. TCF21 forward: AACGACAAATACGAGAACGGGT; reverse: CTCCAGGTACCAAACTCCAAGG. FAP forward: GCTTTGAAAAATATCCAGCTGCC; reverse: ACCACCATACACTTGAATTAGCA. FN forward: ACAACACCGAGGTGACTG AGAC. reverse: GGACACAACGATGGTTCCTGAG. ACTA2 forward: AGAACATGGCATCATCACCA. reverse: GCGTCCAGAGGCA TAGAGAG. POSNT forward: CCCTTGGAAGAGACGGTCAC. reverse: CTCAAAGACTGCTCCTCCCA. Elastin forward: TTCCCCG CAGTTACCTTTCC. reverse: CTAAGCCACCAACTCCTGGG. Ki67 forward: ATTTGCTTCTGGCCTTCCCC. reverse: CCAAACAAG CAGGTGCTGAG. CCND1 forward: CTGATTGGACAGGCATGGGT. reverse: GTGCCTGGAAGTCAACGGTA. FGF2 forward: CC CCAGAAAACCCGAGCGA. reverse: TTCACGGATGGGTGTCTCCG. PDGFRB forward: CAGCTCTGGCCCTCAAAGG. reverse: GAACGAAGGTGCTGGAGACA. BAX forward: AGGGGCCCTTTTGCTTCAG. reverse: TGTCCAGCCCATGATGGTTC. BCL2 forward: GAAGGTTTCCTCGTCCCTGG. reverse: GAAGACCCTGAAGGACAGCC. P53 forward: AGTCTAGAGCCACCGTCCAG. reverse: TCCGGGGACAGCATCAAATC. P21 forward: AGTCAGTTCCTTGTGGAGCC. reverse: CATTAGCGCATCACAGTCGC. GREM1 forward: TAAGCAGACCATCCACGAGG. reverse: GGCAGTTGAGTGTGACCATC. FSP1 forward: CCCTGGATGTGATGGTGTCC. reverse: CGATGCAGGACAGGAAGACA. HSP90AA1 forward: GGTCCTGTGCGGTCACTTAG reverse: TATCTGCACCAGCCTGC AAA HSP90AB1 forward: AACCGCCCTGCTATCTTCTG reverse: ACAAACTCCTTGCCACACCA.

The target mRNA expression levels were normalized to GAPDH levels. GAPDH forward: TGCACCACCAACTGCTTAGC; reverse: GGCATGGACTGTGGTCATGAG. Relative quantization was expressed as fold-induction compared with controls in triplicate of three independent experiments.

Confocal fluorescence microscopy of ECCT cross-sections

Leica SP5 confocal, 63× oil objective, 1.4 mm aperture and 2.5 zoom was used. Fluorescence of ECCT cross-sections was taken using 49% intensity, CTPR390 (excitation: 390 nm, emission: 488 nm), DAPI channel, laser 405 nm, intensity 27%, excitation filter 415 nm, emission filter 500 nm. Seven z-slices were acquired with a step size of 1.13 μm. The images were analyzed using ImageJ software. A median filter was applied to each channel and a maximum intensity z-projection was performed for each channel separately.

Transmission electron microscopy

Control, TGFβ1 and TGFβ1-CTPR390 treated ECCTs were examined for conventional ultrastructural analysis. ECCTs were fixed with 1% paraformaldehyde and 1% glutaraldehyde in 0.1 M phosphate buffer, pH 7.4. Then they were cut in half to get material for TEM and Scanning Electron Microscopy (SEM) analysis. Continuing with the TEM protocol, the ECCTs were rinsed in 0.1 M phosphate buffer, postfixed in 2% osmium tetroxide, dehydrated in ethanol, and embedded in araldite (Durcupan, Fluka, Switzerland). Semi thin sections were used not only as a quality proof to proceed to ultrathin sections but also for quantification, in that case, ultrathin sections were stained with 1% toluidine blue and observed and digitalized with a conventional light microscope (Leica DM1000) and analyzed with ImageJ software.[54] All the analyses were carried out using GraphPad software for Windows. Ultrathin sections were transferred to copper grids and stained with uranyl acetate and lead citrate. Transmission Electron Microscopy (TEM) images of cross-section of ECCT were recorded at an accelerating voltage of 80 kV and with magnifications ranging from 6000× to 29,000× using a GatanUltraScan 100 slow-scan CCD camera and software Gatan.

Scanning electron microscopy

The sectioned ECCTs were fixed in 3% glutaraldehyde, dehydrated with a graded ethanol series, dried by the critical point method, coated with gold in a Fine coat ion sputter JFC-1100 226 (JEOL, Ltd), and observed with an Inspect S microscope (FEI Company) working at 25 kV.

Cellular area, perimeter and layers quantification

To measure the area and perimeter of cells extracted from ECCT, the following procedure was used. First, ECCT samples were dissociated to obtain individual cells, which were then purified and replated for 24 h. After this incubation period, cell images were captured using an Olympus IX81 fluorescence microscope with a 10× UPlanFLN objective. These images were subsequently analyzed with ImageJ software to measure the perimeter and area of the cells. This method provided measurements of cell morphology and spatial organization.

For the measurement of the number of cell layers, various areas within the longitudinal semi-thin sections of the three ECCT groups under study (Control, TGFβ1, and TGFβ1-CTPR390) were analyzed. The superficial cell count was performed covering areas of 4,000 μm^2, while the interior cell count was conducted in areas of 16,000 μm^2. The relativization of the percentages of superficial cells and interior cells of the ECCT was done in relation to each of the analyzed areas.

Cell viability and counting method

Cell parameter values for number, viability, and diameter were obtained using the CASY TTS system, which utilizes three-dimensional counting, electric current exclusion (ECE), and pulse area analysis for accurate measurements. During measurement, cells in either growth media or 5% FBS-containing DPBS were kept on ice. CASY accurately determines cell viability without interference from staining or focusing. Viable cells are identified by their intact cell membranes, which act as a barrier to current, while dead cells are detected by their nuclei due to the lack of membrane resistance.

Assessment of Hsp90 inhibitors in human cardiac fibroblasts

Primary human cardiac fibroblasts (PromoCell, ref: NHCF-V, batch: 22TL122676) were incubated in the presence of TGFβ1 (Santa Cruz Biotechnology, ref: HZ-1011-5UG) at a concentration of 5 ng/mL, and treated with Hsp90 inhibitors at a concentration of 1 μM for 24 h. The inhibitors used were 17-AAG (Santa Cruz Biotechnology, ref: sc-200641, Lot# B2715), Epigallocatechin gallate (EGCG) (Sigma-Aldrich, ref. 0397-05-90, batch: HWI03035), and CTPR390. Following the 24-h incubation, RNA was extracted from the treated fibroblasts as described in the section "quantitative PCR analysis of cell samples". The impact of each treatment on gene expression was analyzed to assess the effects of Hsp90 inhibition on fibroblast response to TGFβ1.

Polarized light imaging of picrosirius red staining samples

Collagen fibers, when organized in a structured and aligned manner, exhibit birefringence or the ability of a material to refract light in two different directions. The birefringence given by the polarized light passing through structured collagen of ECCTs enabled us to distinguish between regions of the ECCT characterized by organized collagen and those with less organized or unstructured collagen. Collagen content in ECCT constructs ($n = 2$/condition: Control, TGFβ1, TGFβ1-CTPR390) was quantified using a Picrosirius Red staining protocol. Briefly, ECCT samples were fixed in 4% formaldehyde, paraffin-embedded, and sectioned into thin 0.5μm cross-sections. Following deparaffinization and rehydration through a graded series of xylene and ethanol washes, sections were stained with 1% Picrosirius red solution (Sirius Red in picric acid). Excess stain was removed by washing, and sections were dehydrated and mounted for subsequent analysis of collagen fiber cross-sectional area. Collagen fibers will be observed as birefringent, i.e., with bright colors ranging from red to yellow-green, depending on their orientation in the field of view. This allowed for the measurement of the cross-sectional areas of the ECCT samples. Polarized light images were acquired using a Zeiss Cell Axio Observer microscope. Transmission imaging was performed with an EC Plan Neofluar 10× air objective (0.3 numerical aperture) and a Zeiss 305 Axiocam, utilizing both brightfield and polarization modes (0° polarizer, 90° analyzer). The total area of ECCT was calculated through transmission image processing, and collagen quantification was achieved by analyzing the positive areas using the open-source software Fiji.[54]

Multiphoton microscopy

The multiphoton imaging technique utilizes nonlinear optical effects to visualize collagen structures in biological tissues. Specifically, it relies on two-photon excitation, where two photons of lower energy combine to excite a fluorophore. In the case of collagen, Second Harmonic Generation (SHG) is the predominant signal observed. Structured collagen, such as that found in organized and aligned fibers, produces a strong and specific SHG signal. This is because the nonlinear optical process is enhanced in highly ordered structures. To detect structured collagen, the Second Harmonic Generation (SHG) nonlinear optical process was employed (n = 3 ECCT per group) using a Zeiss LSM 880 NLO multiphoton laser microscope coupled with a Mai Tai Deep See multiphoton laser. Imaging was performed with a C Apochromat 40× water objective (1.20 numerical aperture). Big2 detectors (Non-Descanned Detectors) were used for image acquisition in the 500–550 nm range, with excitation at 780 nm at 1% power. The image pixel size was set to 0.10 micrometers, with 8-bit resolution.

SAXS imaging

Synchrotron Small-Angle X-ray Scattering (SAXS) imaging was collected at the SAXSMAT[38] beamline in PETRAIII from three groups of ECCT cultivated for 13 days: Control, TGFβ1 (to induce fibrosis) and TGFβ1-CTPR390 groups. ECCTs were extracted from the cultured plate and transferred to the planchettes for their cryopreservation in a 20% BSA freezing media. Then, they were cryofixed in an EM HPM100 High Pressure Freezing System and freeze died following temperature and pressure gradients with a single chamber method in a Chris Alpha 2–4 LSCplus. This generated ECCT samples around 3 mm in diameter and 0.3 mm thick, ready for their study at room temperature. SAXS studies were performed at the P62 SAXSMAT beamline (PETRA III, Hamburg, Germany)[55] with a 12 keV beam focused at 21 × 22 μm^2, and using an Eiger 2 × 9 M detector (in an evacuated flight tube) at a distance of 4.7 m. An ionization chamber before the sample and a beamstop in front of the SAXS detector allowed to monitor primary and transmitted beam intensities (for normalisation purposes). The ECCTs were wrapped and immobilised using Kapton foil, and positioned on a goniometer inside a chamber filled with He (to minimize air background scattering). SAXS maps were acquired from areas between 4 and 6 mm^2 that were continuously raster scanned with a virtual spot size of 20 × 20 μm^2 and 0.2 s dwell time per virtual point of the YZ projections. Each 2D SAXS pattern was transformed to show scattering values between 0° and 360°. Afterward, the one-dimensional SAXS profiles were corrected by self-attenuation, effective exposure time per virtual point, normalized by the incoming flux, and the background signal. The 5^{th} reflection order of collagen ($q \approx 0.48\ nm^{-1}$) was used to reconstruct the collagen intensity, rank-1 tensor maps and degree of orientation as previously described.[41] The degree of orientation values for each ECCTs were normalized to the highest alignment signal among the three ECCTs for clarity. Any pixel with a degree of orientation below 0.15 was considered as an area of relative disoriented collagen. To avoid unwanted beam damage during acquisition, SAXS imaging were performed using dry samples. Yet, due to their size, the different ECCTs studied needed to be cut and folded inside the aluminum capsules used for cryofixation under high pressure, and freeze dried before analysis. Unfortunately, this hampered recognition of the different sections from the ETCs within the images generated. Initially, the intensity of collagen alignment in each 20 × 20 μm^2 pixel of the ECCTs was normalized to the highest alignment signal among the three ECCTs, to obtain a value of relative degree of orientation (between 0 and 1). Any pixel with a relative degree of orientation below 0.15 was considered as an area of relative disoriented collagen.

QUANTIFICATION AND STATISTICAL ANALYSIS

Data presented in this study were expressed as means ± SEM for n = 3–24 ECCT per group depending on the assay performed. p values (*$p < 0.05$, **$p < 0.005$, ***$p < 0.0005$, ****$p < 0.0001$). All datasets were tested for normal distribution using the Shapiro-Wilk test. p-values for datasets following a normal distribution were determined using the parametric ANOVA with Tukey's multiple comparison test. For datasets that did not follow a normal distribution, p-values were determined using the non-parametric Mann-Whitney test.